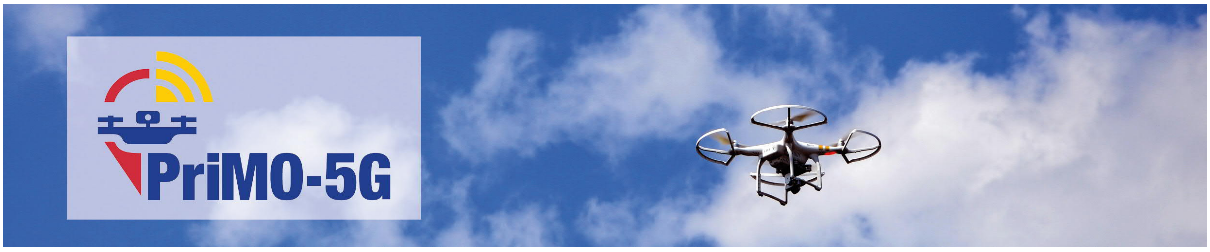

Project Title	Virtual Presence in Moving Objects through 5G
Project Acronym	PriMO-5G
Grant Agreement No	815191
Instrument	Research and Innovation Action
Topic	The PriMO-5G project addresses the area of “a) Focus on mmWave and super broadband services” in the call “EUK-02-2018: 5G” of the Horizon 2020 Work Program 2018-2020.
Start Date of Project	01.07.2018
Duration of Project	36 Months
Project Website	https://primo-5g.eu/

D3.2 - INTERMEDIATE REPORT ON THE 5G TRANSCEIVER DESIGN AND ADAPTIVE BEAMFORMING

Work Package	WP3, Advanced radio technologies
Lead Author (Org)	Author (Institution)
Contributing Author(s) (Org)	Sang-Hyun Park (YU), Gee-Yong Suk (YU), Soo-Min Kim (YU), Changmin Lee (YU), Tae-Hun Jung (YU), Hong bae Jeon (YU), Dong Soo Jun (YU), Chan-Byoung Chae (YU), Kwang Soon Kim (YU), Eui Whan Jin (YU), Kwanghoon Lee (YU)Achim Nahler (NI), Walter Nitzold (NI), Abdo Nasser Ali Gaber (NI), Hyungsik Han (KAIST), Seonyong Kim (KAIST), Namshik Kim (KAIST), Seongbae Jun (KAIST), Hyuncheol Park (KAIST)
Due Date	30.04.2020, M22
Date	30.04.2020
Version	4.0 (submitted

Dissemination Level

☒ PU: Public
☐ PP: Restricted to other programme participants (including the Commission)
☐ RE: Restricted to a group specified by the consortium (including the Commission)
☐ CO: Confidential, only for members of the consortium (including the Commission)

The work described in this document has been conducted within the project PriMO-5G. This project has received funding from the European Union’s Horizon 2020 research and innovation programme under grant agreement No 815191. The project is also supported by the Institute for Information & communications Technology Promotion (IITP) grant funded by the Korea government (MSIT) (No.2018-0-00170, Virtual Presence in Moving Objects through 5G). The dissemination of results herein reflects only the author’s view, and the European Commission, IITP and MSIT are not responsible for any use that may be made of the information it contains.

Versioning and contribution history

Version	Date	Authors	Notes
1.0	30.03.2020	Sang-Hyun Park (YU), Gee-Yong Suk (YU), Soo-Min Kim (YU), Changmin Lee (YU), Tae-Hun Jung (YU), Hong bae Jeon (YU), Dong Soo Jun (YU), Chan-Byoung Chae (YU), Kwang Soon Kim (YU), Eui Whan Jin (YU), Kwanghoon Lee (YU)Achim Nahler (NI), Walter Nitzold (NI), Abdo Nasser Ali Gaber (NI), Hyungsik Han (KAIST), Seonyong Kim (KAIST), Namshik Kim (KAIST), Seongbae Jun (KAIST), Hyuncheol Park (KAIST)	Initial table of contents, and content contributions
2.0	31.03.2020	Sang-Hyun Park (YU), Gee-Yong Suk (YU), Soo-Min Kim (YU), Changmin Lee (YU), Tae-Hun Jung (YU), Hong bae Jeon (YU), Dong Soo Jun (YU), Chan-Byoung Chae (YU), Kwang Soon Kim (YU), Eui Whan Jin (YU), Kwanghoon Lee (YU)Achim Nahler (NI), Walter Nitzold (NI), Abdo Nasser Ali Gaber (NI), Hyungsik Han (KAIST), Seonyong Kim (KAIST), Namshik Kim (KAIST), Seongbae Jun (KAIST), Hyuncheol Park (KAIST)	Final content contributions and draft completion for internal review
3.0	29.04.2020	Sang-Hyun Park (YU), Gee-Yong Suk (YU), Soo-Min Kim (YU), Changmin Lee (YU), Tae-Hun Jung (YU), Hong bae Jeon (YU), Dong Soo Jun (YU), Chan-Byoung Chae (YU), Kwang Soon Kim (YU), Eui Whan Jin (YU), Kwanghoon Lee (YU)Achim Nahler (NI), Walter Nitzold (NI), Abdo Nasser Ali Gaber (NI), Hyungsik Han (KAIST), Seonyong Kim (KAIST), Namshik Kim (KAIST), Seongbae Jun (KAIST), Hyuncheol Park (KAIST)	Revisions across whole document after internal review comments
4.0	30.04.2020	Edward Mutafungwa (AALTO)	Final editorial check prior to submission

Disclaimer

PriMO-5G has received funding from the European Union’s Horizon 2020 research and innovation programme under grant agreement No 815191. The project is also supported by the Institute for Information & communications Technology Promotion (IITP) grant funded by the Korea government (MSIT) (No.2018-0-00170, Virtual Presence in Moving Objects through 5G). The dissemination of results herein reflects only the author’s view, and the European Commission, IITP and MSIT are not responsible for any use that may be made of the information it contains.

Table of Contents

List of Tables

List of Figures

Executive Summary

The title of Deliverable D3.2 is the intermediate report on the 5G transceiver design and adaptive beamforming. This deliverable is the second report from WP3 mmWave radio technologies, which aims to investigate important radio technology concepts for 5G NR. To that end, D3.2 includes research and development of new innovative transmission concepts using 5G mmWave frequencies. This intermediate report focuses on developing radio technologies that contribute to meet operational, functional, and technical requirements inspired by the PriMO-5G firefighting use cases (specified previously as part of work in WP1 Scenarios, architecture, economic and regulatory analysis). Therefore, in addressing those use case requirements, this deliverable reports on initial research in PriMO-5G on enhanced 5G radio access technologies that could be classified into three thematic areas, namely: novel transceiver design, waveform design, and advanced beamforming.

A novel mmWave transceiver architecture based on 5G NR requirements is shown. The components to achieve such as system are characterized, and performance measurements of the complete mmWave front-end with 5G NR compliant PHY layer signals are presented. These results indicate suitable EVM performance for the Primo-5G use cases. In terms of waveform design, we designed waveforms and prototype filters for QAM-FBMC considering an MMSE receiver filter. The proposed filters are designed to have a superior self-SINR under the condition of the linear receiver, and we confirmed that the filters show the best performance with the design intent through simulation results. In addition, the formulations of the linear system and self-SINR equations for QAM-FBMC showed a simpler representation than that of the previously complex QAM-FBMC system; therefore, we identified the possibility of applying popular signal processing technology directly to QAM-FBMC in the future. Second, we proposed USFDMA as a new waveform in anticipation that it would be challenging to satisfy the target service condition in D1.1 with OFDMA and GFDM. USFDMA is a suitable waveform to satisfy the URLLC service condition because filtering and resource allocation are possible for each carrier so that it is possible to reduce interference and OOBE and maximize spectral efficiency. In terms of advanced beamforming, first, we proposed a beam tracking algorithm based on ABP-EKF for mmWave MIMO systems in mobile environments. With the modified ABP structure, the proposed algorithm has better beam tracking performance than ABP based angle estimation in the low SNR region, and the MSE performance can be improved by EKF. Second, we analyzed the beam-squint phenomenon in RF lens array and phased array for an ultra-wideband mmWave system. To find the causes of BQ in the RF lens, we separated two cases with assumptions. The leading cause is the antenna beampattern difference of single patch antenna that does not support ultra-wideband if the material of the lens has stable permittivity over frequency. To verify these results, we proposed DPBQ as a KPI. Third, Since the mmWave band has a strong directivity and is vulnerable to blockage, an accurate estimation technique is required for analog beamforming. Conventional techniques require many RF chains to achieve accuracy so that it is difficult to apply. We proposed a technique to estimate the offset by calculating the monopulse ratio using a sum beam and difference beam, respectively, when transmitting data and CP. It showed that it uses lower overhead than the conventional scheme, but can achieve similar performance.

List of Acronyms

Acronym	Definition
5G	Fifth-Generation Mobile Network
ABP	Auxiliary beam pair
AD	Angle distortion
ADC	Analog-to-digital converter
AoA	Angle of arrival
AoD	Angle of departure
AWGN	Additive white Gaussian noise
BB	Digital baseband
BER	Bit error rate
BQ	Beam-squint
BS	Base station
CP-OFDM	Cyclic prefix-orthogonal frequency division multiplexing
CSI	Channel state information
DAC	Digital-to-analog converter
DFT	Discrete Fourier transform
DL	Downlink
DPBQ	Degraded power over beam squint
EKF	Extended kalman filter
EPA	Extended ITU pedestrian A
EVA	Extended ITU vehicular A
EVM	Error Vector Magnitude
FBMC	Filter-bank multi-carrier
FPGA	Field Programmable Gate Array
gNB	Next Generation NodeB
GPS	Global Positioning System
IF	Intermediate Frequency
LO	Local oscillator
MAC	Medium Access Control

MCU	Microcontroller
MIMO	Multiple-input multiple-output
MUSIC	Multiple signal classification
MMIC	Monolithic Microwave Integrated Circuit
MMSE	Minimum mean square error
mmWave	Millimeter wave
MS	Mobile station
MSE	Mean square error
OFDM	Orthogonal Frequency-Division Multiplexing
OOBE	Out-of-band emission
OQAM	Offset-QAM
PAPR	Peak-to-Average Power Ratio
PD	Power difference
PHY	Physical Layer
PSD	Power spectral density
RF	Radio-frequency
RRC	Radio Resource Control
RSS	Received signal strength
RX	Receiver
self-SINR	Self-signal-to-noise-and-interference ratio
SINR	Signal-to-interference-plus-noise ratio
SNR	Signal-to-noise ratio
SPI	Serial Peripheral Interface
TDD	Time division duplex
TDD	Time division duplex
TX	Transmitter
UART	Universal Asynchronous Receiver Transmitter
UE	User Equipment
UL	Uplink
ULA	Uniform linear array

URLLC	Ultra-reliable low-latency communications
USFDMA	Universal spatio-frequcney division multiple access
USRP	Universal Software Radio Peripheral
VCO	Voltage-controlled oscillator
VR	Virtual Reality
WP	Work Package

1 Introduction

1.1 Purpose and Scope

The title of deliverable 3.2 is an intermediate report on the 5G transceiver design and adaptive beamforming. In this deliverable, we write a result compilation of 5G mmWave Radio Transceiver design and adaptive beam steering and tracking that are not contained in D3.1. To enable the overall vision of an end-to-end communication system for immersive video services, different enabling technologies have to be incorporated into the PriMO-5G system architecture. Also, the forest fighting scenario A and use case A1 from Deliverable D1.1 are the target applications for mmWave transmission. In these scenarios, many video capturing drones are used for monitoring a fire scene. We should redesign the radio transceiver design containing MAC and PHY layers. Besides, adaptive beamforming is needed in scenarios where drones cross each cell. The ultimately deliverable aims to Gbps throughput as well as sub-ms latency using a high bandwidth system for mmWave carrier frequencies. Also, waveform design being suitable for PriMO-5G is contained.

1.2 Structure of the document

D3.2 consists of three sections, such as novel transceiver design, waveform design, and advanced beamforming. Section 2 is about a novel transceiver design. We introduce a mmWave transceiver suitable for the PriMo-5G use case. To accommodate the requirements currently incorporated into the 5G NR standard, investigations on a novel transceiver design are carried out and presented in Section 2. Section 3 is about the waveform design suitable for transceiver design. In section 3.1, we used FBMC to resolve the drawback of the side-lobe leakage and cyclic prefix of CP-OFDM. Besides, waveform design and prototype filter considering the MMSE received filters are introduced. In section 3.2, we proposes new multiple access technology, universal spatio-frequcney division multiple access (USFDMA), which can satisfy the requirements of URLLC for 5G service for Ultra-reliable low-latency communications. Section 4 is about advanced beamforming. In section 4.1, we supposed ABP design for angle estimation and beam tracking algorithm in high mobility environment. A method of AoA tracking via an extended Kalman filter is also introduced. In section 4.2, In the hybrid-beamforming method, we analyzed and compared the difference between conventional phased array and RF lens array in the beam-squint perspective. In section 4.3, we introduce hybrid beamforming using a monopulse ratio that used in the radar system to suppressed conventional AoA/AoD estimation error and sounding protocol overheads.

1.3 Relationship to other project outcomes

Deliverable 3.2 will provide input on the planned demonstration activities in D5.1~5.3 of WP5 Testbed and demonstration, which will include some of the experimental implementations of the enhanced radio access technologies and concepts introduced in this document. In the D5.2, based on WP3 D3.1~D3.3, Demo form European partners, Korean partners and intracontinental system will be presented.

2 Novel transceiver design

An important technology building block to fulfil the requirements of PriMO-5G use cases is the integration of mmWave transmission schemes with beam management capabilities. While a tremendous amount of work has been shown on the theoretical beam management and beam selection side, a practical implementation that utilizes 5G NR PHY and upper layer designs is the focus of this contribution. The work introduces a novel system architecture utilizing NI USRP SDR systems which are integrated with active antenna array technology. The subsequent sections give an overview on this architectural approach and shed light on the 5G NR related RF requirements for a mmWave system and how the new system architecture can fulfil these requirements.

2.1 NI mmWave transceiver system

This section deals with description of the targeted mmWave transceiver system provided by NI. In Sec 2.1.1 the targeted system parameters are given and the RF part of the system architecture is described. Sec. 2.1.2 provides information about the used IF and mmWave components including their key performance data which are relevant to meet the required system performance. Performance considerations are addressed in Sec.2.1.3. Finally, Sec. 2.1.4 gives an outlook on the integration activities planned for the upcoming reporting period.

2.1.1 System architecture

Table 2.1-1 gives an overview about the system parameters targeted with the mmWave transceiver system provided by NI. In particular, it is worth mentioning that the targeted frequency range covers partially the band n257 specified by 3GPP (see Tab. 5.2-1 of [3GPP20-38101]), which serves as pioneering band for European mmWave activities. Further, it is targeted to fullfill on UE side the requirements for power class 3, (see Sec. 6.2.1.3 of [3GPP20-38101]). That implies a maximum TX output power of 23 dBm.

Table 2.1-1 Targeted system parameters

Frequency	26.5 – 28.5 GHz
TX output power	23 dBm
Carrier Bandwidth	100 MHz
Subcarrier Spacing	120 kHz Data; 240 kHz SSB (Synchronisation Signal Block)
Duplex mode	TDD
TDD scheme	8:2 DDDFDDDFUU (F=10d+2g+2u)
Modulation	OFDM: Up to 64 QAM
DL Channels/Signals	PDSCH, PDCCH, PBCH, PSS, SSS, DMRS, PT-RS
UL Channels/Signals	PUSCH, PUCCH, PRACH, DMRS, PT-RS, SRS

Figure 2.1-1**Error! Reference source not found.** shows the architecture of the RF subsystem which is in the focus of this deliverable. mmWave components will be integrated with NI USRP devices. Hence, the NI USRP serves as IF transmitter/receiver which is connected to up-/downconverters to shift the IF signal into the RF frequency range. Active antenna arrays are used to radiate the RF signals. For the UE side, an 2x8 active antenna array will be used, whereas an 8x8 active antenna array will be used on the gNB side. It is noted that the 2x8 active antenna array has already an integrated up- and downconverter. The control of the active antenna arrays will be done in real-time via the USRP using UART and SPI protocols. The next section will describe the mmWave components in more detail.

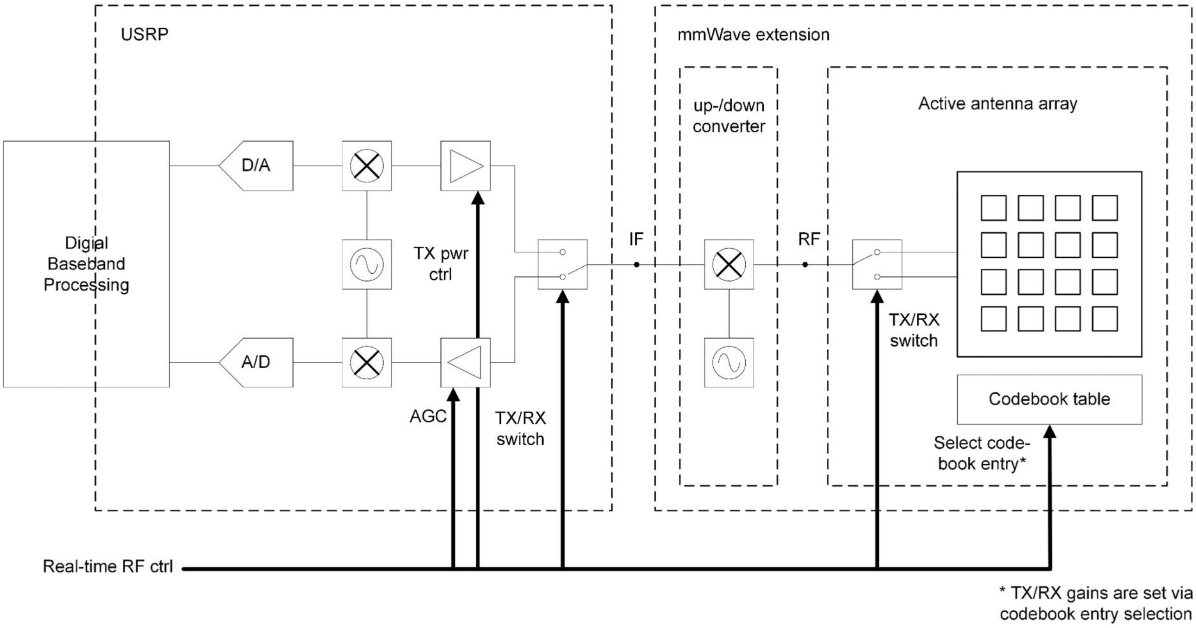

Figure 2.1-1 Architecture of RF subsystem

2.1.2 *Description of mmWave components*

2.1.2.1 USRP

The USRP-2954 provides an integrated hardware and software solution. The hardware architecture combines two extended-bandwidth daughterboard slots covering 10 MHz – 6 GHz with up to 160 MHz of instantaneous real-time bandwidth, multiple high-speed interface options (PCIe, dual 10 GigE, dual 1 GigE), and a large user-programmable Kintex-7 FPGA. The XC7K410T FPGA provides high-speed connectivity between all major components within the device including radio frontends, host interfaces, and DDR3 memory. The USRP-2954 is equipped with a GPS-disciplined 10 MHz OCXO reference clock. The GPS disciplining provides a high-accuracy frequency reference, and global timing alignment to within 5 ppb when synchronized to the GPS system. The USRP-2954 RIO device is a LabVIEW FPGA target, which supports creating custom FPGA implementations and configuring the device using Instrument Design Libraries. Table 2.1-2 shows the key performance data of USRP 2954-R. The front panel of NI USRP-2954-R is shown in Figure 2.1-2. More information can be found under [NI-USRP17].

Table 2.1-2 USRP 2954-R key performance data

Transmitter		Receiver	
Number of channels	2	Number of channels	2
Frequency range	10 MHz … 6 GHz	Frequency range	10 MHz … 6 GHz
Max. output power	17 … 20 dBm	Max. input power	-15 dBm
TX gain range	0 … 31.5 dB	RX gain range	0 … 37.5 dB
Frequency accuracy	25 ppb	Frequency accuracy	25 ppb
DAC resolution	16 bit	ADC resolution	14 bit

DAC SFDR	80 dB	ADC SFDR	88 dB
		Noise figure	5 … 7 dB

Figure 2.1-2 USRP-2954 Front Panel

2.1.2.2 Up-/downconverters

The RF 5G Mixer is a 24 GHz to 28 GHz up / down converter with an integrated phase locked loop synthesizer. It contains a MMIC mixer, a synthesizer with integrated VCO, a differential 100 MHz reference TCXO, and a loop filter. The up- and downconverter is going to be used on the gNB side in combination with the 8x8 active antenna array. Table 2.1-3 shows the specifications of up / down converter. Figure 2.1-3 shows the up and down converter.

Table 2.1-3 Key performance data for up- and downconverter to/from 28 GHz

Upconverter		Downconverter	
IF	DC … 4 GHz	IF	DC … 4 GHz
RF	24 … 28 GHz	RF	24 … 28 GHz
Conversion loss	Typically 14 dB	Conversion loss	Typically 15 dB
IF input 1dB compression point	6 dBm	RF input 1dB compression point	14 dBm
Isolation IF to RF	Typically 41 dB	Isolation RF to IF	Typically 29 dB

Figure 2.1-3 The 28G Up and Down Converter

2.1.2.3 Active antenna arrays for gNB and UE

The millimeter wave antenna arrays are designed for the 28G band. They cover a frequency range of 26.5 to 28.5 GHz and have a linear polarization. Only the TDD operation mode is supported. The beam widths can be configured programmatically. On the gNB side, an 8x8 active antenna array will be used while on the UE side, a 2x8 active antenna array will be used. The antenna array of gNB does not include the LO and the up / down converter; their hardware is separated as it is described in Sec. 2.1.2.2. The 2x8 active antenna array of UE is occupied with an integrated up/down converter, an LO and a microcontroller (MCU) to achieve beamforming functionality. Both provide a 2D electronic beam scan. The control of the active antenna arrays will be done via the USRP using UART and SPI protocols for the 8x8 active antenna array and using UART for the 2x8 active antenna array. Table 2.1-4 shows the specifications of the gNB and UE antenna arrays. The front panel of the 8x8 active antenna array is shown in Figure 2.1-4.

Table 2.1-4 Key performance data for 8x8 and 2x8 active antenna arrays

8x8 active antenna array (for gNB)		2x8 active antenna array (for UE)	
RF	26.5 … 28.5 GHz	RF	26.5 … 28.5 GHz
Input 1 dB compression point	0 dBm	Input 1 dB compression point	-5 dBm
TX/RX gain	50 dB	TX/RX gain	40 dB
Polarization	Vertical linear	Polarization	Vertical linear
Beam coverage	+/- 60° AZ/EL each	Beam coverage	+/-60° AZ, +/-15° EL
Default beam width	15°	Beam width	15°
Number of simultanous beams	Single radiation beam	Number of simultanous beams	Single radiation beam
Beam update rate	3 us	Beam update rate	100 us
RF Interface	TDD only	RF Interface	TDD only
Control Interfaces	UART, SPI	Control Interfaces	UART

Figure 2.1-4 The 8x8 Active Antenna Array

2.1.3 Performance considerations

2.1.3.1 Level plan, link budget

Based on key performance data of the components mentioned in Sec. 2.1.2, level plans and a link budget will be established. Based on the link budget, an estimate of the covered range will be provided.

For the level plans, downlink and uplink directions need to be considered. For the TX path, achieving a maximum TX output power of 23 dBm is the main requirement. For the downlink TX path, upconverter insertion loss and maximum TX gain of the 8x8 active antenna gain need to be considered. Further, it has to be ensured that OFDM signal power is below input 1 dB compression points of the upconverter and active antenna array considering a headroom of 12 dB as typical value for PAPR of an OFDM signal. Specific numbers for the downlink TX path can be found in Table 2.1-5.

Table 2.1-5 Level plan for downlink TX path of 8x8 active antenna array

USRP	Upconverter		Active antenna array	
IF TX out pwr	**TX gain**	**RF TX out pwr**	**Ant TX gain**	**Ant TX out pwr**
OFDM: -12 dBm	-15 dB	-27 dBm	50 dB	OFDM: 23 dBm

For the uplink TX path, the same level plan approach is taken into account but it needs to be considered that the 2x8 active antenna array already includes the upconverter. Uplink TX path specific numbers can be found in Table 2.1-6.

Table 2.1-6 Level plan for uplink TX path of 2x8 active antenna array

USRP	Active antenna array including upconverter	
IF TX out pwr	**TX gain**	**Ant TX out pwr**
OFDM: -17 dBm	40 dB	OFDM: 23 dBm

For the RX path, minimum RX sensitivity and maximum RX input power level need to be considered. Minimum RX sensitivity for power class 3 devices shall be -85 dBm or below as specified in Tab. 7.3.2.3-1 of [3GPP20-38101] for system with a component carrier bandwidth of 100 MHz. Maximum RX input power level shall be at least -25 dBm as given in Tab 7.4-1 of [3GPP20-38101].

For the RX path, input 1 dB compression point for the downconverter and maximum input power for the USRP shall be considered to avoid unwanted non-linear distortions. Table 2.1-7 and Table 2.1-8 provide the numbers for the downlink RX path and the uplink RX path, respectively, assuming an PAPR of 12 dB for the OFDM signal.

Table 2.1-7 Level plan for downlink RX path of 2x8 active antenna array

Active antenna array including downconverter		USRP
Ant RX in pwr	**RX gain**	**IF RX in pwr**
OFDM: -85 dBm	40 dB	-45 dBm
OFDM: -30 dBm	3 dB	-27 dBm

Table 2.1-8 Level plan for uplink RX path of 8x8 active antenna array

Active antenna array				USRP
Ant RX in pwr	**Ant RX gain**	**RF RX out pwr**	**RX gain**	**IF RX in pwr**
OFDM: -85 dBm	50 dB	-35 dBm	-15 dB	-50 dBm

OFDM: -25 dBm	13 dB	-12 dBm	-15 dB	-27 dBm

Based on Friis transmission formula [F46], a simple free-space path loss model can be derived and the covered ranges can be estimated assuming a certain TX output power and a certain RX sensitivity level. Considering Friis, we assume that the free-space path loss can be calculated as FSPL(dB) = $20\log_{10}(d) + 20\log_{10}(f) - 147.55$ whereas d is the distance in meters between gNB and UE, f is the carrier frequency in Hz. Table 2.1-9 provides values for estimated ranges having a carrier frequency of 28 GHz.

Table 2.1-9 Link budget and estimated ranges

TX pwr (EIRP @ TX beam peak)	RX sensitivity (EIS @ 0 dBi RX antenna gain)			
	-85 dBm	**-75 dBm**	**-65 dBm**	**-55 dBm**
20 dBm	d = 151.4 m	d = 47.9 m	d = 15.1 m	d = 4.8 m
15 dBm	d = 85.2 m	d = 26.9 m	d = 8.5 m	d = 2.7 m
10 dBm	d = 47.9 m	d = 15.1 m	d = 4.8 m	d = 1.5 m
5 dBm	d = 26.9 m	d = 8.5 m	d = 2.7 m	d = 0.8 m

2.1.3.2 Performance measurements

Figure 2.1-5 shows the EVM performance of the RF subsystem described in this subsection. All measurements have been taken over the air. The system has been parametrized as follows: IF = 2 GHz, RF = 26 GHz and a component carrier bandwidth = 100 MHz. The 5GNR 3GPP Rel-15 compliant waveform has a subcarrier spacing = 120 kHz, 64QAM as modulation scheme and the usage of PTRS has been enabled. A measured averaged EVM of approximately 4% would allow the usage of 64QAM as modulation scheme while spectrum emission mask is kept.

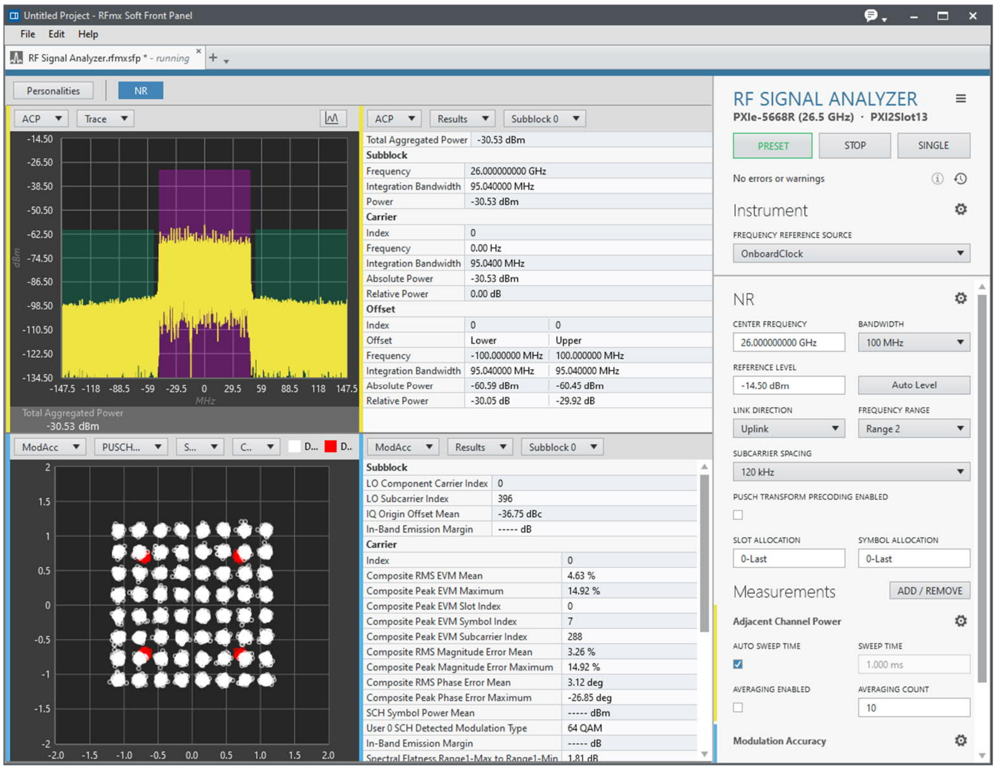

Total Aggregated Power	-30.53 dBm	
Subblock		
Frequency	26.000000000 GHz	
Integration Bandwidth	95.040000 MHz	
Power	-30.53 dBm	
Carrier		
Index	0	
Frequency	0.00 Hz	
Integration Bandwidth	95.0400 MHz	
Absolute Power	-30.53 dBm	
Relative Power	0.00 dB	
Offset		
Index	0	0
Offset	Lower	Upper
Frequency	-100.000000 MHz	100.000000 MHz
Integration Bandwidth	95.040000 MHz	95.040000 MHz
Absolute Power	-60.59 dBm	-60.45 dBm
Relative Power	-30.05 dB	-29.92 dB

Subblock	
LO Component Carrier Index	0
LO Subcarrier Index	396
IQ Origin Offset Mean	-36.75 dBc
In-Band Emission Margin	----- dB
Carrier	
Index	0
Composite RMS EVM Mean	4.63 %
Composite Peak EVM Maximum	14.92 %
Composite Peak EVM Slot Index	0
Composite Peak EVM Symbol Index	7
Composite Peak EVM Subcarrier Index	288
Composite RMS Magnitude Error Mean	3.26 %
Composite Peak Magnitude Error Maximum	14.92 %
Composite RMS Phase Error Mean	3.12 deg
Composite Peak Phase Error Maximum	-26.85 deg
SCH Symbol Power Mean	----- dBm
User 0 SCH Detected Modulation Type	64 QAM
In-Band Emission Margin	----- dB
Spectral Flatness Range1-Max to Range1-Min	1.81 dB

RF SIGNAL ANALYZER
PXIe-5668R (26.5 GHz) · PXI2Slot13

No errors or warnings

Instrument

FREQUENCY REFERENCE SOURCE: OnboardClock

NR

CENTER FREQUENCY: 26.000000000 GHz
BANDWIDTH: 100 MHz
REFERENCE LEVEL: -14.50 dBm
LINK DIRECTION: Uplink
FREQUENCY RANGE: Range 2
SUBCARRIER SPACING: 120 kHz
PUSCH TRANSFORM PRECODING ENABLED: ☐
SLOT ALLOCATION: 0-Last
SYMBOL ALLOCATION: 0-Last

Adjacent Channel Power

AUTO SWEEP TIME: ☑
SWEEP TIME: 1.000 ms
AVERAGING ENABLED: ☐
AVERAGING COUNT: 10

Modulation Accuracy

Figure 2.1-5 Snapshot of EVM measurement having IF = 2 GHz and RF = 26 GHz

2.1.4 Outlook

The functionality and performance of the mmWave components towards the Primo-5G goals has been shown in this section. Integration of these mmWave components into an already available L1 – L3 solution will be the main activity for the upcoming and final reporting period. Addition of beam management functionality will be the focus. More specifically, algorithms will be implemented for

- initial beam establishment
- beam adjustment and
- beam failure recovery.

That implies that means to

- configure UE measurements and UE measurement reporting
- execute those measurements and report back from UE to gNB and to
- execute actions on gNB and UE based on the measurements and measurement reports, respectively,

need to be implemented. In order to achieve those functionalities, are careful assessment needs to be done what the impact of those features to the existing PHY layer including real-time RF control, the MAC layer and the RRC layer for both UE and gNB will be.

3 Waveform design

mmWave transmission is an important technology that meets the requirements of PriMO-5G use cases. This work introduces waveform design for mmWave systems. The subsequent sections give a design of QAM-FBMC waveforms to resolve the disadvantages of CP-OFDM, …

3.1 QAM-FBMC with MMSE receiver

In this Section we focus on the design of QAM-FBMC waveforms. FBMC has been considered an alternative waveform to resolve the disadvantages of CP-OFDM. The advantages of FBMC includes such as high out-band emission characteristics and the loss of spectral efficiency [BBC+14].

Instead of maintaining the orthogonality in the real domain through offset-QAM (OQAM), QAM-FBMC uses QAM which increases the risk of giving up some degree of orthogonality in the complex domain. A QAM-FBMC filter designed to be nonorthogonal may degrade performance, but signal processing in the complex domain can easily be applied to QAM-FBMC in a way similar to CP-OFDM. The remaining major issue of QAM-FBMC is the need to design the system and filters to minimize the non-orthogonality that causes performance degradation.

For QAM-FBMC, a matched filter is not suitable as a receiver filter. Instead, a filter following the MMSE criterion can minimize interference and maximizes SINR, and be a more suitable linear receiver for QAM-FBMC [P94]. In addition, by designing the prototype filter considering the MMSE receiver filter, we can achieve the system close to orthogonal waveforms as possible, and also expect to significantly mitigate the BER performance degradation due to the non-orthogonal filters.

For system model, we denote M as a number of subcarriers, L as an overlapping factor for the filtering in the frequency domain, and $N = LM$ as a number of upsampled frequency points, as shown in Figure 3.1-1. To formulate the stacked representation of overlapped transmit signal, we define the k-th stacked data symbol vector $\bar{\mathbf{d}}[k]$ as follows:

$$\bar{\mathrm{d}}[\boldsymbol{k}] = [\mathrm{d}[\boldsymbol{k}-\boldsymbol{L}]^{\mathbf{T}}, \dots, \mathrm{d}[\boldsymbol{k}]^{\mathbf{T}}, \dots, \mathrm{d}[\boldsymbol{k}+\boldsymbol{L}-\mathbf{1}]^{\mathbf{T}}]^{\mathbf{T}}, \tag{3-1}$$

where $\mathbf{d}[k]$ is a k-th data vector with the m-th element, $d_m[k]$, which is a QAM data symbol. The $\bar{\mathbf{d}}[k]$ includes the $(k-L+1)$-th to the $(k+L-1)$-th data symbols considering the overlap-and-sum structure, and includes $(k-L)$-th symbol to consider interference from channel delays.

From the $\bar{\mathbf{d}}[k]$, a k-th transmitted signal $\bar{\mathbf{x}}[k]$ in the stacked representation can be written as

$$\bar{\mathrm{x}}[\boldsymbol{k}] = \bar{\mathrm{G}}_{\boldsymbol{f}} \bar{\mathrm{d}}[\boldsymbol{k}]. \tag{3-2}$$

And $\bar{\mathbf{G}}_f$ is a stacked pulse-shaping fliter matrix of size $(M+N) \times 2N$ as

$$\bar{\mathrm{G}}_{\boldsymbol{f}} = \left[\mathrm{G}_{\boldsymbol{f}}^{(-\boldsymbol{L})}, \dots, \mathrm{G}_{\boldsymbol{f}}^{(\mathbf{0})}, \dots, \mathrm{G}_{\boldsymbol{f}}^{(\boldsymbol{L}-\mathbf{1})}\right]. \tag{3-3}$$

The $\mathbf{G}_f^{(l)}$ is constructed by m-th column $\mathbf{g}_m^{(l)}$ with $(n+M)$-th element $g_m^{(l)}[n]$, and $g_m^{(l)}[n]$ is defined in $n = -M, \dots, N-1$ range as follows:

$$\begin{gathered} \boldsymbol{g}_{\boldsymbol{m}}^{(\boldsymbol{l}\geq\mathbf{0})}[\boldsymbol{n}] = \begin{cases} \boldsymbol{p}_{\mathbf{0}}[\boldsymbol{n}]\boldsymbol{e}^{\left(\boldsymbol{j}\mathbf{2}\boldsymbol{\pi}\frac{\boldsymbol{m}(\boldsymbol{n}-\boldsymbol{l}\boldsymbol{M})}{\boldsymbol{M}}\right)}, & \boldsymbol{n} = \boldsymbol{l}\boldsymbol{M}, \dots, \boldsymbol{N}-\mathbf{1}, \\ \mathbf{0}, & \textbf{otherwise}, \end{cases}. \\ \boldsymbol{g}_{\boldsymbol{m}}^{(\boldsymbol{l}<\mathbf{0})}[\boldsymbol{n}] = \begin{cases} \boldsymbol{p}_{\mathbf{0}}[\boldsymbol{n}]\boldsymbol{e}^{\left(\boldsymbol{j}\mathbf{2}\boldsymbol{\pi}\frac{\boldsymbol{m}(\boldsymbol{n}-\boldsymbol{l}\boldsymbol{M})}{\boldsymbol{M}}\right)}, & \boldsymbol{n} = -\boldsymbol{M}, \dots, \boldsymbol{N}+\boldsymbol{l}\boldsymbol{M}-\mathbf{1}, \\ \mathbf{0}, & \textbf{otherwise}, \end{cases} \end{gathered} \tag{3-4}$$

where $p_0[n]$ is a prototype filter defined in $n = 0, \dots, N-1$ range. By equation (3-2), we can now represent the signal that has passed the overlap-and-sum structure without sum operation.

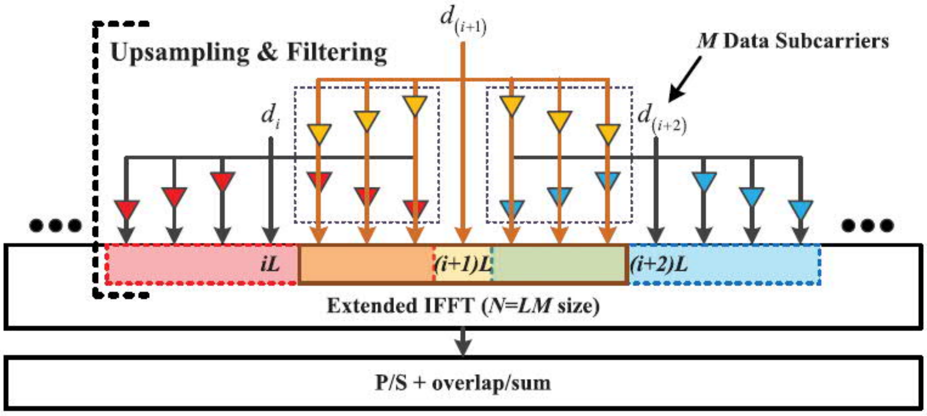

Figure 3.1-1 The QAM-FBMC transmitted signal structure (L = 4)

To represent the time-domain channel for the stacked vector $\bar{\mathbf{x}}[k]$, we define $(N + M) \times (N + M)$ channel convolution matrix $\mathbf{H}$, and the each column of the matrix is given by shift of the channel impulse response with L_c taps as follows:

$$[\mathrm{H}]_{(:,\boldsymbol{m})} = \mathbf{shift}\left\{\left[\boldsymbol{h}_{\mathbf{0}} \cdots \boldsymbol{h}_{\boldsymbol{L_c}-\mathbf{1}}\ \mathbf{0}_{\boldsymbol{N}+\boldsymbol{M}-\boldsymbol{L_c}}\right]^{\mathbf{T}}, \boldsymbol{m}-\mathbf{1}\right\}. \tag{3-5}$$

The k-th received signal vector $\mathbf{y}[k]$ of size $N \times 1$ can be written as

$$\mathrm{y}[\boldsymbol{k}] = \mathrm{TH}\bar{\mathrm{G}}_{\boldsymbol{f}}\bar{\mathrm{d}}[\boldsymbol{k}] + \mathrm{n}[\boldsymbol{k}], \tag{3-6}$$

where $\mathbf{T} = [\mathbf{0}_{N\times M}\ \mathbf{I}_N]$ is a time-domain slice matrix to extract the samples in the k-th received window, and $\mathbf{n}[k]$ is the AWGN vector with complex Gaussian distribution of $\mathrm{CN}(\mathbf{0}, \sigma_n^2\mathbf{I}_N)$. If we simply consider linear receiver process as a filter of size $M \times N$, we can represent the k-th detected data symbol as follows:

$$\tilde{\mathrm{d}}[\boldsymbol{k}] = \mathrm{Q}_{\boldsymbol{f}}^{\mathbf{H}}\mathrm{H}_{\mathbf{eff}}\bar{\mathrm{d}}[\boldsymbol{k}] + \mathrm{Q}_{\boldsymbol{f}}^{\mathbf{H}}\mathrm{n}[\boldsymbol{k}], \tag{3-7}$$

where $\mathbf{H}_{\mathrm{eff}} = \mathbf{TH}\bar{\mathbf{G}}_f$, and $\mathbf{Q}_f$ is a receiver filter matrix that we will formulate by the MMSE criterion in section 3.1.1. Overall, we show the QAM-FBMC transceiver structure in stacked matrix representation in Figure 3.1-2.

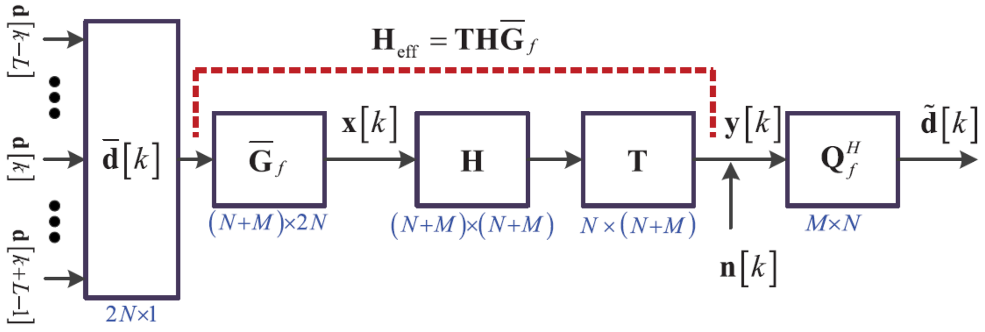

Figure 3.1-2 The stacked matrix representation of the QAM-FBMC system

3.1.1 Receiver filter by MMSE criterion

For the receiver filter $\mathbf{Q}_f$, we formulate a MMSE problem of the k-th detected data symbol as follows:

$$\hat{\mathrm{Q}}_{\boldsymbol{f}}^{(\mathbf{MMSE})} = \mathop{\mathbf{arg\,min}}_{\mathrm{Q}_{\boldsymbol{f}}} \mathbf{E}\left[\|\mathrm{e}\|_{\mathbf{2}}^{\mathbf{2}}\right] = \mathop{\mathbf{arg\,min}}_{\mathrm{Q}_{\boldsymbol{f}}} \mathbf{E}\left[\left\|\tilde{\mathrm{d}}[\boldsymbol{k}] - \mathrm{S}\bar{\mathrm{d}}[\boldsymbol{k}]\right\|_{\mathbf{2}}^{\mathbf{2}}\right] \tag{3-8}$$

$$= \mathbf{arg}\min_{\mathrm{Q}_f} \mathbf{E}\left[\left\|\left(\mathrm{Q}_f^{\mathbf{H}}\mathrm{H}_{\mathbf{eff}}\bar{\mathrm{d}}[\boldsymbol{k}] + \mathrm{Q}_f^{\mathbf{H}}\mathrm{n}[\boldsymbol{k}]\right) - \mathrm{S}\bar{\mathrm{d}}[\boldsymbol{k}]\right\|_2^2\right],$$

where $\mathbf{S} = \left[\mathbf{0}_{M\times N}, \dots, \mathbf{I}_M, \dots, \mathbf{0}_{M\times(L-1)N}\right]$ is a matrix for extracting the k-th data symbol from the stacked vector $\bar{\mathbf{d}}[k]$. The expectation of the squared-error becomes

$$\mathbf{E}\left[\|\mathrm{e}\|_2^2\right] = \mathbf{tr}\left\{\left(\mathrm{Q}_f^{\mathbf{H}}\mathrm{H}_{\mathbf{eff}} - \mathrm{S}\right)\left(\mathrm{H}_{\mathbf{eff}}^{\mathbf{H}}\mathrm{Q}_f - \mathrm{S}^{\mathbf{H}}\right)\right\}\boldsymbol{\sigma}_d^2 + \mathbf{tr}\left\{\mathrm{Q}_f\mathrm{Q}_f^{\mathbf{H}}\right\}\boldsymbol{\sigma}_n^2, \tag{3-9}$$

where we assume that the covariance of the stacked data symbol vector is $\mathrm{E}\left[\bar{\mathbf{d}}\bar{\mathbf{d}}^{\mathrm{H}}\right] = \sigma_d^2\mathbf{I}_{2N}$, and the data symbols and AWGN are uncorrelated. We can rewrite the (9) as follows:

$$\begin{aligned}\mathbf{E}\left[\|\mathrm{e}\|_2^2\right] &= \mathbf{tr}\left\{\mathrm{Q}_f^{\mathbf{H}}\mathrm{A}\mathrm{Q}_f\left(\mathrm{Q}_f^{\mathbf{H}}\mathrm{H}_{\mathbf{eff}} - \mathrm{S}\right)\left(\mathrm{H}_{\mathbf{eff}}^{\mathbf{H}} - \mathrm{S}^{\mathbf{H}}\right)\right\}\boldsymbol{\sigma}_d^2 + \mathbf{tr}\left\{\mathrm{Q}_f\mathrm{Q}_f^{\mathbf{H}}\right\}\boldsymbol{\sigma}_n^2 \\ &= \mathbf{tr}\left\{\left(\mathrm{C}^{\mathbf{H}}\mathrm{Q}_f - \mathrm{C}^{-1}\mathrm{B}\right)^{\mathbf{H}}\left(\mathrm{C}^{\mathbf{H}}\mathrm{Q}_f - \mathrm{C}^{-1}\mathrm{B}\right)^{\mathbf{H}} + \mathrm{e}_{\mathbf{min}}\right\},\end{aligned} \tag{3-10}$$

where $\mathbf{A} = \sigma_d^2\mathbf{H}_{\mathrm{eff}}\mathbf{H}_{\mathrm{eff}}^{\mathrm{H}} + \sigma_n^2\mathbf{I}_N = \mathbf{C}\mathbf{C}^{\mathrm{H}}$, $\mathbf{B} = \mathbf{H}_{\mathrm{eff}}\mathbf{S}^{\mathrm{H}}\sigma_d^2$, $\mathbf{e}_{\min} = \sigma_d^2\mathbf{I}_{2N} - \mathbf{B}^{\mathrm{H}}\mathbf{A}^{-1}\mathbf{B}$. Since $\mathbf{e}_{\min}$ is not related to $\mathbf{Q}_f$, and the left term is the form of Frobenius norm, the equation (3-10) becomes convex. Therefore, the minimum point is $\mathbf{C}^{\mathrm{H}}\mathbf{Q}_f - \mathbf{C}^{-1}\mathbf{B} = 0$, and the solution of the MMSE problem becomes

$$\widehat{\mathrm{Q}}_f^{(\mathbf{MMSE})} = \mathrm{C}^{-\mathbf{H}}\mathrm{C}^{-\mathbf{1}}\mathrm{B} = \mathrm{A}^{-\mathbf{1}}\mathrm{B} = \left(\mathrm{H}_{\mathbf{eff}}\mathrm{H}_{\mathbf{eff}}^{\mathbf{H}} + \frac{\boldsymbol{\sigma}_n^2}{\boldsymbol{\sigma}_d^2}\mathrm{I}_N\right)^{-\mathbf{1}}\mathrm{H}_{\mathbf{eff}}\mathrm{S}^{\mathbf{H}}. \tag{3-11}$$

3.1.2 Waveform design with MMSE receiver

Consider the QAM-FBMC waveform design problem as the optimization of the prototype filter. We assume that the single prototype filter for practical transmission structure, and prototype filter is complex modulated by the frequency coefficients as follows:

$$\boldsymbol{p}_0(\boldsymbol{n}) = -\sum_{k=-(K-1)}^{K-1} \boldsymbol{q}_k e^{j2\pi\frac{kn}{N}} = \boldsymbol{q}_0 + \mathbf{2}\sum_{k=1}^{K-1} \mathbf{Re}\left[\boldsymbol{q}_k e^{j2\pi\frac{kn}{N}}\right], \tag{3-12}$$

where the coefficients are conjugated symmetric as $q_k = q_{-k}^*$, and K is a number of non-zero coefficients in the one-sided frequency domain. Therefore, to design the waveform, we optimize the frequency coefficient vector $\mathbf{q}$ of size K with k-th element q_k ($k = 0, \dots, K-1$).

Before formulating a filter design problem, we need to update the existing average self-SINR expression in [KHP17] using the stacked representation, and the self-SINR $\Upsilon(\sigma_n^2, \mathbf{q})$ can be defined as follows:

$$\boldsymbol{\Upsilon}(\boldsymbol{\sigma}_n^2, \mathrm{q}) = \frac{\mathbf{1}}{\boldsymbol{M}}\sum_{i=0}^{M-1} \frac{\left|\left[\mathrm{Q}_f^{\mathbf{H}}\mathrm{H}_{\mathbf{eff}}\right]_{(i,i+N)}\right|^2}{\sum_{j=0, j\neq i+N}^{2N-1}\left|\left[\mathrm{Q}_f^{\mathbf{H}}\mathrm{H}_{\mathbf{eff}}\right]_{(i,j)}\right|^2 + \left[\mathrm{Q}_f^{\mathbf{H}}\mathrm{Q}_f\right]_{(i,i)}\boldsymbol{\sigma}_n^2}, \tag{3-13}$$

where the receiver filter $\mathbf{Q}_f$ can be $\mathbf{Q}_f = \mathbf{Q}_f^{(\mathrm{MF})} = \mathbf{T}\mathbf{G}_f^{(0)}$ for matched filter, and $\mathbf{Q}_f = \mathbf{Q}_f^{(\mathrm{MMSE})}$ for the MMSE filter as shown in (11).

With reference to [KHP17], the optimization problem can be formulated with the spectral and time localization constraints as follows:

$$\begin{aligned}&\mathbf{maximize}_{\mathrm{q}}\ \boldsymbol{\Upsilon}(\boldsymbol{\sigma}_n^2, \mathrm{q}) \\ &\mathbf{subject\ to}\ \boldsymbol{\sigma}_t < \boldsymbol{\epsilon}_t, \left|\boldsymbol{q}_0 + \mathbf{2}\sum_{k=1}^{K-1}\mathbf{Re}[\boldsymbol{q}_k]\right| < \boldsymbol{\epsilon}_0, \\ &\qquad \left|\sum_{k=1}^{K-1}\boldsymbol{k}\mathbf{Im}[\boldsymbol{q}_k]\right| < \boldsymbol{\epsilon}_1, \left|\sum_{k=1}^{K-1}\boldsymbol{k}^2\mathbf{Re}[\boldsymbol{q}_k]\right| < \boldsymbol{\epsilon}_2,\end{aligned} \tag{3-14}$$

where σ_t is a time dispersion parameter defined as

$$\boldsymbol{\sigma_t} = \frac{\mathbf{1}}{\boldsymbol{N}}\sqrt{\sum_{\boldsymbol{n}=\mathbf{0}}^{\boldsymbol{N}-\mathbf{1}}\left(\boldsymbol{n}-\sum_{\boldsymbol{n}=\mathbf{0}}^{\boldsymbol{N}-\mathbf{1}}\boldsymbol{n}|\boldsymbol{p}_{\mathbf{0}}[\boldsymbol{n}]|^{\mathbf{2}}\right)^{\mathbf{2}}|\boldsymbol{p}_{\mathbf{0}}[\boldsymbol{n}]|^{\mathbf{2}}}\,. \qquad (3\text{-}15)$$

Since the prototype filter problem is non-convex with the high-dimensional variables, thus the filter design may require a high computational complexity. After the prototype filter is successfully designed, the system can simply utilize the designed filter at no extra design cost, however it is very difficult to redesign this filter every time the channel changes. Therefore, this deliverable assumes that the prototype filter is predesigned before the transmission. On the other hand, in equation (3-13), the self-SINR depends on the channel $\mathbf{H}$ and the noise variance of the receiver σ_n^2. Since it is difficult to consider an actual channel value or a particular channel model when pre-designing the prototype filter, we assume that the channel is AWGN with $\mathbf{H}_{\text{eff}} = \mathbf{T}\overline{\mathbf{G}}_f$. About the noise variance of the receiver σ_n^2, we set the target SNR to 15, 30, 50, and infinite dB, and design the prototype filter considering the MMSE receiver filter for each target SNR which denoted as G15, G30, G50, and Ginf, respectively.

Since the optimization problem (3-14) cannot be solved with convex optimization tool, we design the prototype filters with $K = 15$ frequency domain filter taps and $L = 4$ oversampling factor through the pattern search algorithm which is a global optimization technique [AD04]. The pattern search algorithm basically performs a polling process, which updates the optimal point by adding or subtracting each vector element from a given vector point. We set the self-SINR function $\Upsilon(\sigma_n^2, \mathbf{q})$ for the frequency coefficient vector q as the fitness function, the fall-off rate conditions as the linear constraint, and the time dispersion condition as the nonlinear constraint. The tolerance parameters of each constraint are set to $\epsilon_0 = 0.01$ and $\epsilon_1 = \epsilon_2 = \epsilon_t = 0.01$.

The proposed filter design results are described in Table 3.1-1, and summarized in Table 3.1-2. Figure 3.1-3 shows the self-SINR performances of the each prototype filter with SNR variation. As intended in the filter design, the Type G15 and G30 filters exhibit the highest self-SINR at 15dB and 30dB SNR, respectively. Overall, the proposed prototype filters for the MMSE receiver filter show better performances than the reference filters for the matched receiver filter. Specifically, comparing the reference filter Type 2 and Type G30 at the SNR of 30dB, the self-SINR can achieve the performance improvement of 4.25dB, and in the case of 50dB SNR, the Type G50 improves the self-SINR of 5.98dB.

Table 3.1-1 Proposed filter coefficients in the frequency domain

	Type G15	Type G30	Type G50	Type Ginf
	Only real coefficients			
q_0	+1.0000	+1.0000	+1.0000	+1.0000
q_1	-0.8660	-0.9591	-0.9988	-0.9655
q_2	+0.6662	+0.7533	+0.7628	+0.7616
q_3	-0.3932	-0.3915	-0.3597	-0.4422
q_4	+0.0066	+0.0844	+0.1029	+0.1859
q_5	+0.2122	+0.2388	+0.1849	+0.0610
q_6	-0.2680	-0.4369	-0.3509	-0.1987
q_7	+0.1702	+0.2274	+0.2325	+0.1965
q_8	-0.0050	-0.0648	-0.1383	-0.1652
q_9	-0.1571	-0.0774	-0.0504	-0.0025
q_{10}	+0.1871	+0.2961	+0.3059	+0.1745
q_{11}	-0.0910	-0.2442	-0.2552	-0.1267
q_{12}	+0.0091	+0.1152	+0.1836	+0.1106
q_{13}	+0.1623	-0.0077	-0.2207	-0.1760
q_{14}	-0.1315	-0.0317	+0.1033	+0.0889

Table 3.1-2 Comparison of the proposed filters

	[YKK+12]	[KHP+17]	Proposed			
Type	2	C	G15	G30	G50	Ginf
Receiver filter	Matched		MMSE			
Target SNR (dB)	∞	∞	15	30	50	∞
K(taps)	15	15	15	15	15	15
$\Upsilon(0, \mathbf{q})$ (dB)	19.2	17.4	22.8	24.9	25.4	25.4
Fall-off rate	$\lvert\omega\rvert^{-4}$	$\lvert\omega\rvert^{-5}$	$\lvert\omega\rvert^{-5}$	$\lvert\omega\rvert^{-5}$	$\lvert\omega\rvert^{-5}$	$\lvert\omega\rvert^{-5}$
σ_t	0.197	0.083	0.077	0.078	0.075	0.064
Coefficient	Complex	Real	Real	Real	Real	Real

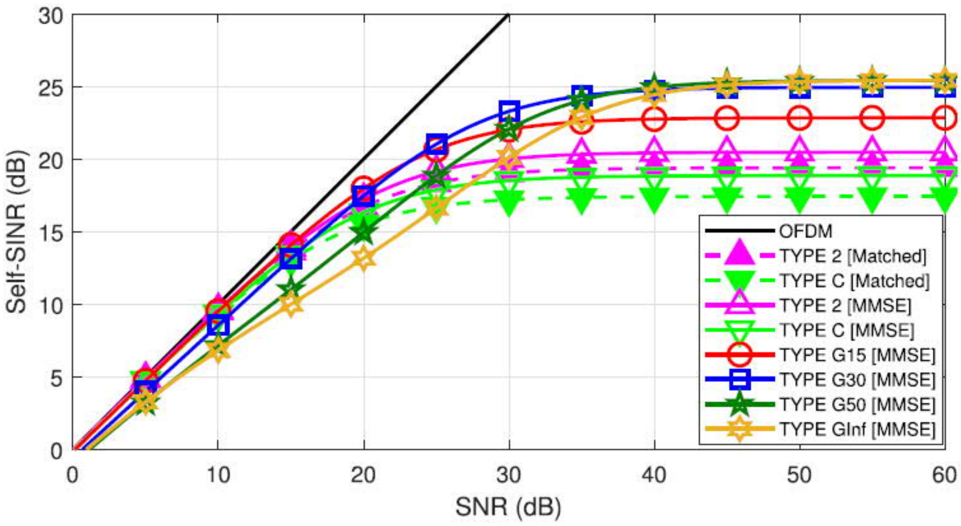

Figure 3.1-3 The self-SINR comparisons of the designed prototype filters with SNR variation.

In what follows we compare the performances of the designed prototype filters, which are presented in Table II. For reference filters with matched receiver filter, we use a single-tap MMSE equalizer in the upsampled frequency domain. Also, we consider the performances of the reference filters with MMSE receiver filter, which is same as the process of the proposed prototype filter.

The common simulation parameters are $L = 4, M = 128, \sigma_d^2 = 1$, 16-QAM/64-QAM, 2GHz carrier frequency, and 15 kHz subcarrier spacing. The channel models of the simulation are AWGN, EPA, and EVA [E-UTRA08].

In Figure 3.1-4, Figure 3.1-5, and Figure 3.1-6, we compare the probability of bit error (BER) performances between the reference filters with matched receiver filter and the proposed filters with the MMSE receiver filter. In the simulation, as mentioned above, we can see that the prototype filters with higher self-SINR show better BER performances as expected, and the performances of the proposed filters are significantly enhanced than the reference filters. As shown in Figure 3.1-4, the Type G30 filter with the highest self-SINR at 30dB SNR shows the best performance in AWGN. And in EPA and EVA channels which require higher SNR, Type G50 and GInf show slightly better BER performances than Type G30. Overall, we can expect that the Type G30 filter performs well in most of the scenarios, so we expect it to be usable in general situation. Additionally, we check the BER performances of the reference filters with MMSE receiver filter. Even if the signal with the reference filters is received through

MMSE filter, the reference filters show the slightly better performances than the matched receiver, but still worse than the proposed filter because it is not designed to use the MMSE filter.

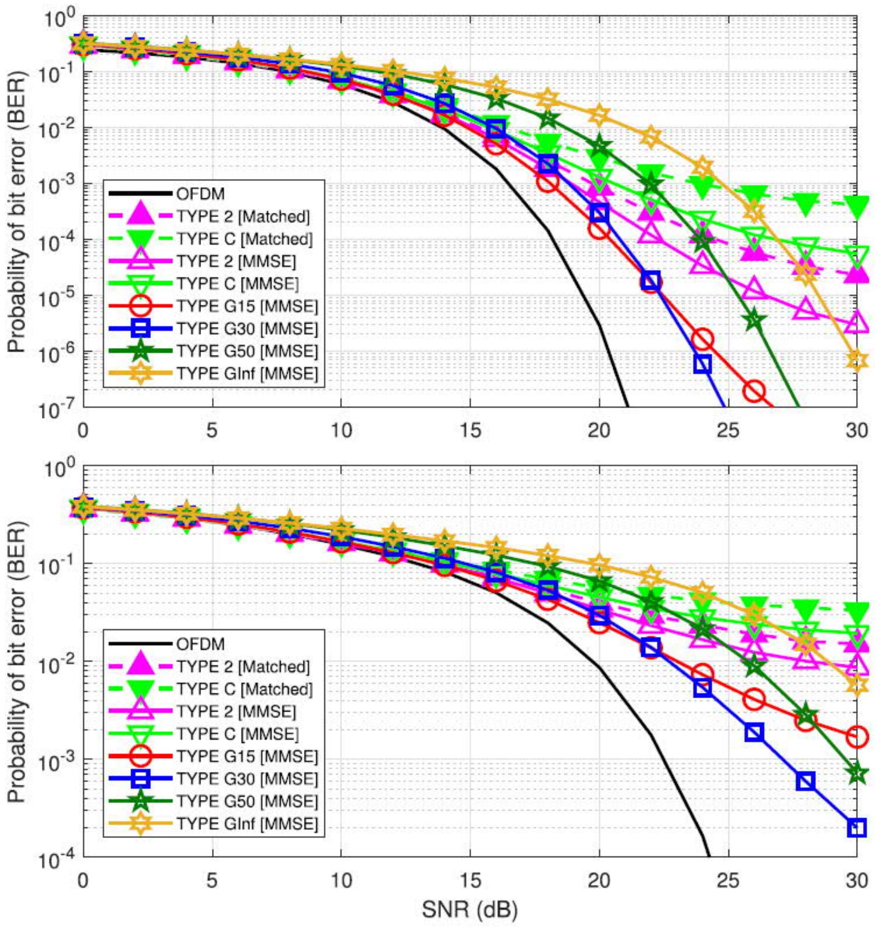

Figure 3.1-4 The BER performance comparisons in the AWGN channel with 16-QAM (top) and 64-QAM (bottom).

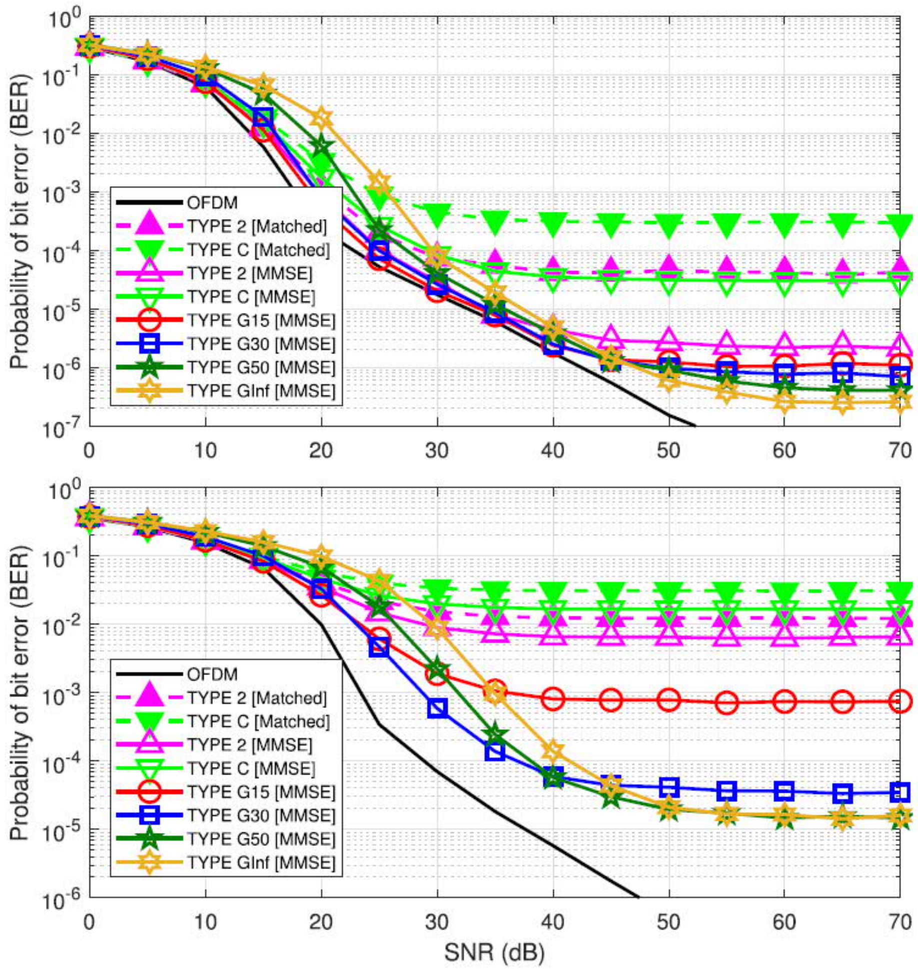

Figure 3.1-5 The BER performance comparisons in the EPA channel with 16-QAM (top) and 64-QAM (bottom).

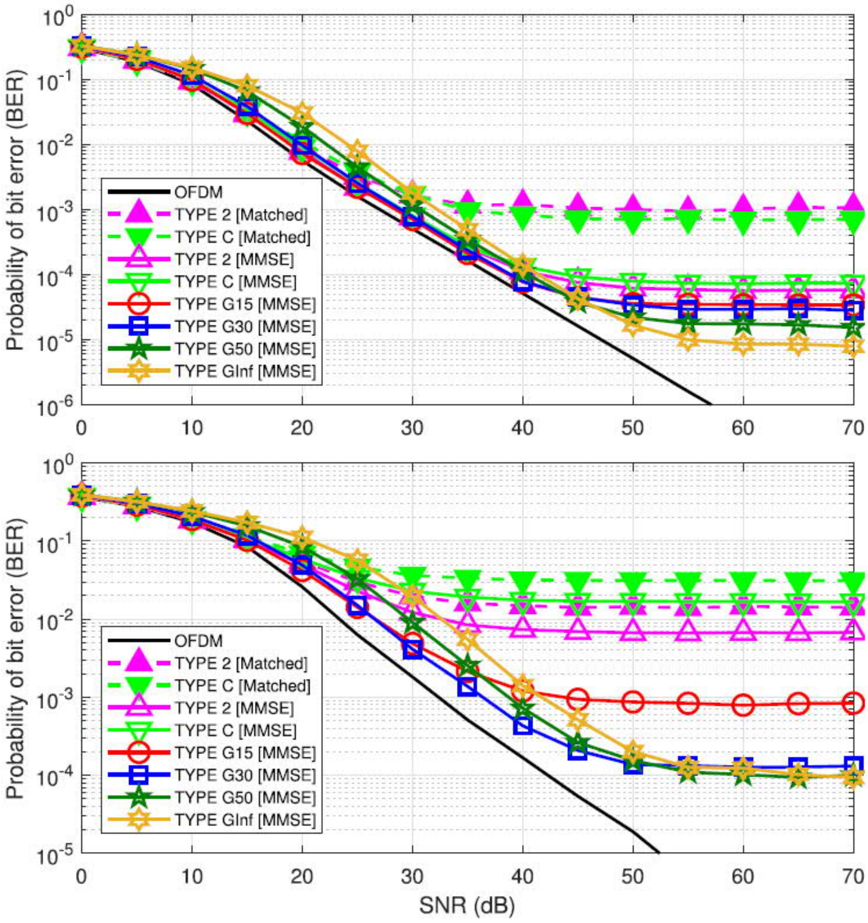

Figure 3.1-6 The BER performance comparisons in the EVA channel with 16-QAM (top) and 64-QAM (bottom).

The most important part in these BER performance results is that the performance degradation of the reference filter compared to OFDM can be significantly mitigated through the proposed prototype filter and MMSE receive structure. Specifically, by the proposed filter and receiver, we can reduce the residual interference so that QAM-FBMC can achieve 10^{-5} uncoded BER performance in high modulation order. In particular, this MMSE receiver works in the linear system instead of complex nonlinear operations such as successive cancellation, and it can be realizable when QAM-FBMC is used in a realistic environment.

Additionally, we can confirm that the designed prototype filters assuming AWGN channel show almost the same performance trends as for AWGN, even if BER simulations are performed on the fading channel models. In the practical system, if the QAM-FBMC transmitter knows or predicts the received SNR, the system can use the pre-designed prototype filters corresponding to the target SNR, which may exhibit the best BER performance. Therefore, if the QAM-FBMC system utilizes the pre-designed prototype filters appropriately, we can expect the good performance even considering the practical channel and varying SNR at the receiver. Figure 3.1-7 shows the PSD of the prototype filters for comparing the spectral confinement characteristics. As we can expect from Table 3.1-2, the Type C and the proposed filters all show the almost same PSD, with a good spectral confinement of $|\omega|^{-5}$, the Type 2 has a medium spectral confinement with a fall-off rate of $|\omega|^{-4}$, and OFDM shows the worst characteristic.

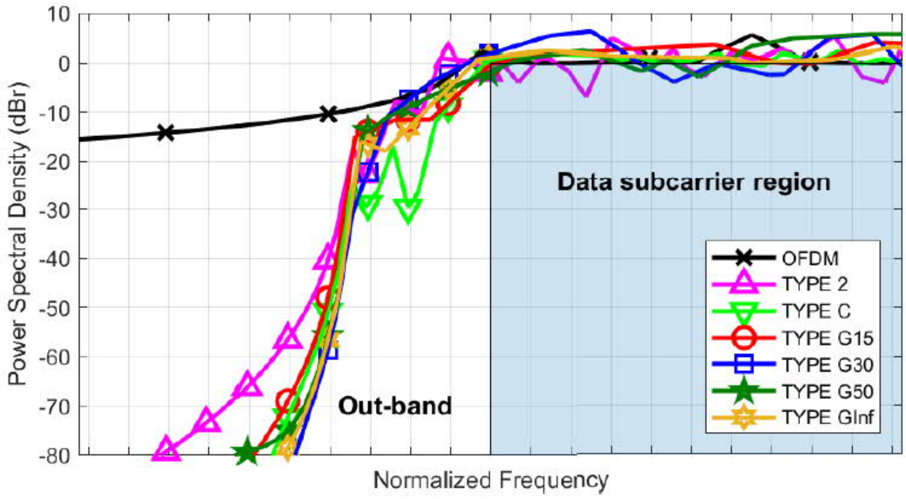

Figure 3.1-7 The comparison of PSD between OFDM and QAM-FBMC filters.

3.2 Design Waveform for mmWave

3.2.1 Universal Spatio-Frequency Division Multiple Access (USFDMA)

Ultra-reliable low-latency communications (URLLC) is the most interesting new service category in 5G to support mission-critical services. In order to get high reliability in a wireless fading channel environment, it is requires a large amount of diversity with a coexistence of different waveforms and multiple access schemes within one carrier, according to various traffic characteristics. We propose new multiple access technology, universal spatio-frequcney division multiple access (USFDMA), which can satisfy the requirements of URLLC for 5G service. The proposed waveform technique is available for time-varying multiple access with spatial-frequency filter.

USFDMA is a kind of filtered multicarrier that allows a low out-of-band emission (OOBE) so that it does not interfere other simultaneously multiplexed waveforms and has robustness to synchronization error. It uses blockwise filters with block size according to the resource allocation for each user so that it provides orthogonality among different subcarriers allocated to different users. Also USFDMA allows multiple layers in the spatial domain so that arbitrary resource allocation in the spatio-frequency domain is possible. In order to maximize the spectral efficiency and connectivity while satisfying the challenging latency and reliability requirements in URLLC services, a user-specific spatio-frequency filter is employed by combining a precoding filter in the spatial domain and the pre-equalizer in the frequency domain with the knowledge of the channel state information (CSI), which can be obtained by using the channel reciprocity of the time division duplex (TDD) and the symmetricity in the traffic characteristics. At the receiver, a spatio-frequency post processing is also applied. Figure 3.2-1 shows the transceiver design of USFDMA.

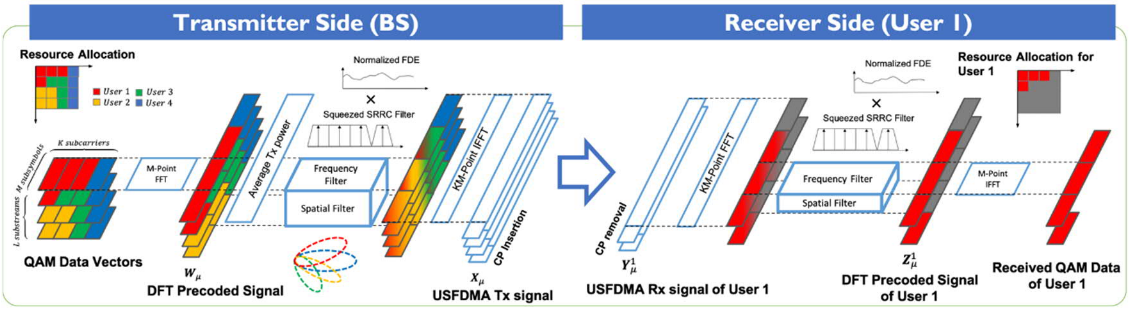

Figure 3.2-1 Transceiver Design of USFDMA.

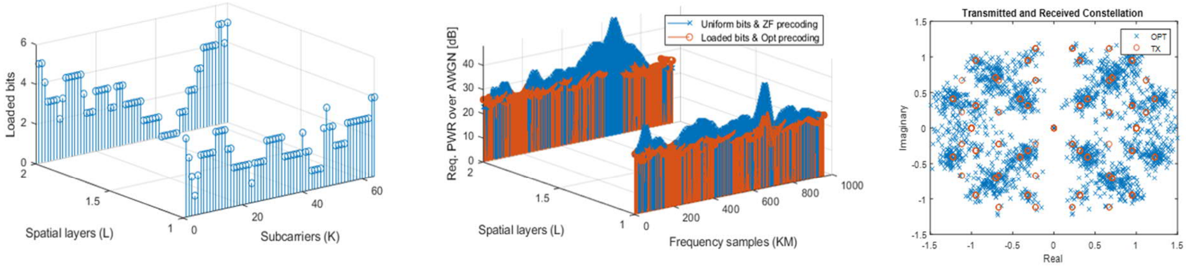

Loaded bits per RB

Req. power comparison

Constellation (Tx, Rx)

Figure 3.2-2 SW Link-Level Simulation

In software link-level simulation, joint optimization of spatio-frequency filter and bit-loading can minimize transmission power required to satisfy URLLC QoS compared to zero-forcing beamforming with uniform bit-loading. This simulation assumes Rayleigh fading and it will expand to mmWave and geometric characteristic.

4 Advanced beamforming

4.1 Robust beam tracking algorithm in mobile environments

Efficient beam estimation and tracking algorithm based on AoA are required for enabling mmWave communications in mobile environments. In this Section we focus on the problem of robust beam tracking for mmWave MIMO systems. Figure 4.1-1 shows the narrowband MIMO system model of uplink channel with beamforming transceiver structure using a single RF chain for easy of implementation. MS and BS are equipped with N and M antenna elements, respectively.

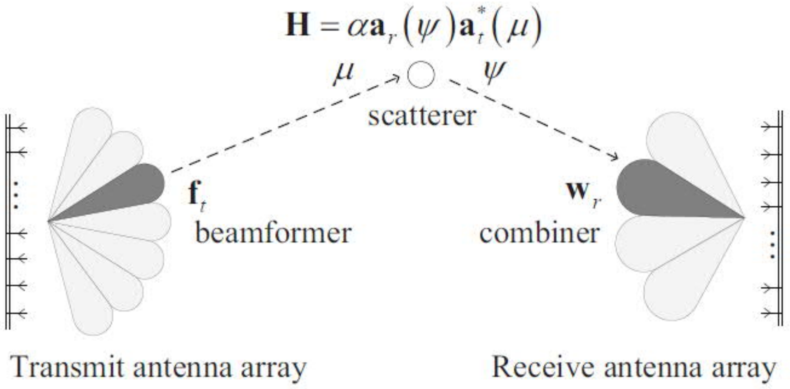

Figure 4.1-1 mmWave MIMO system with beamforming transceiver structure using single RF chain.

In mmWave MIMO channel, the paths are limited in sparse directions due to large path loss and highly directional nature of high frequency signals. In this paper, we model the mmWave MIMO channel with complex path gain, transmit array response vector, receive array response vector, the AoD at the MS, and the AoA at the BS. We consider the time-varying mmWave channel model, at time k, as following:

$$\mathrm{H}[\boldsymbol{k}] = \sum_{\boldsymbol{n=1}}^{\boldsymbol{N_p[k]}} \boldsymbol{\alpha_n}[\boldsymbol{k}]\mathrm{a}_{\boldsymbol{r}}(\boldsymbol{\phi_n}[\boldsymbol{k}])\mathrm{a}_{\boldsymbol{t}}^*(\boldsymbol{\theta_n}[\boldsymbol{k}]), \tag{4-1}$$

where $N_p[k]$ is the number of paths, $\alpha_n[k] \in \mathbb{C}$ is the path gain, $\phi_n[k]$ and $\theta_n[k]$ are the AoA and AoD of the n-th, respectively. $\mathbf{a}_t(\cdot) \in \mathbb{C}^{N\times 1}$ and $\mathbf{a}_r(\cdot) \in \mathbb{C}^{M\times 1}$ are the transmit and receive array response vectors, respectively. We assume 2D model so that we only consider ULAs with antenna spacing of half wavelength at both the transmitter and receiver. The array response vector of ULAs at transmitter is expressed as

$$\mathrm{a}_{\boldsymbol{t}}(\boldsymbol{\theta}) = \frac{\mathbf{1}}{\sqrt{\boldsymbol{N}}}\left[\mathbf{1}, \boldsymbol{e}^{\boldsymbol{j}\frac{2\pi}{\lambda}\boldsymbol{d_t}\sin\boldsymbol{\theta}}, \dots, \boldsymbol{e}^{\boldsymbol{j}\frac{2\pi}{\lambda}(\boldsymbol{N}-\mathbf{1})\boldsymbol{d_t}\sin\boldsymbol{\theta}}\right]^{\mathbf{T}}, \tag{4-2}$$

where λ is a wavelength corresponding to the operating carrier frequency, and d_t is a distance between the adjacent antenna elements at transmitter. We can rewrite the array response vector at transmitter by using transmit spatial frequency $\mu \triangleq \frac{2\pi}{\lambda} d_t \sin\theta$ as follows:

$$\mathrm{a}_{\boldsymbol{t}}(\boldsymbol{\mu}) = \frac{\mathbf{1}}{\sqrt{\boldsymbol{N}}}\left[\mathbf{1}, \boldsymbol{e}^{\boldsymbol{j\mu}}, \dots, \boldsymbol{e}^{\boldsymbol{j}(\boldsymbol{N}-\mathbf{1})\boldsymbol{\mu}}\right]^{\mathbf{T}}. \tag{4-3}$$

Similarly, the array response vector at receiver is expressed as

$$\mathrm{a}_{\boldsymbol{r}}(\boldsymbol{\phi}) = \frac{\mathbf{1}}{\sqrt{\boldsymbol{M}}}\left[\mathbf{1}, \boldsymbol{e}^{\boldsymbol{j}\frac{2\pi}{\lambda}\boldsymbol{d_r}\sin\boldsymbol{\phi}}, \dots, \boldsymbol{e}^{\boldsymbol{j}\frac{2\pi}{\lambda}(\boldsymbol{M}-\mathbf{1})\boldsymbol{d_r}\sin\boldsymbol{\phi}}\right]^{\mathbf{T}}, \tag{4-4}$$

$$\mathrm{a}_{\boldsymbol{r}}(\boldsymbol{\psi}) = \frac{\mathbf{1}}{\sqrt{\boldsymbol{M}}}\left[\mathbf{1}, \boldsymbol{e}^{\boldsymbol{j\psi}}, \dots, \boldsymbol{e}^{\boldsymbol{j}(\boldsymbol{N}-\mathbf{1})\boldsymbol{\psi}}\right]^{\mathbf{T}}, \tag{4-5}$$

where d_r is a distance between the adjacent antenna elements at receiver, and $\psi \triangleq \frac{2\pi}{\lambda} d_r \sin\phi$ is the receive spatial frequency.

Commonly, the mmWave channel has sparse property, and we can assume that its property makes the paths to be likely separated from each other. Accordingly, only the single path falls into the main beam direction [VVH16]. Hence, we restrict to 2D single-path model for the sake of simplicity. Then the single path mmWave channel is expressed as

$$\boldsymbol{H}[\boldsymbol{k}] = \boldsymbol{\alpha}[\boldsymbol{k}]\mathrm{a}_{\boldsymbol{r}}(\boldsymbol{\psi}[\boldsymbol{k}])\mathrm{a}_{\boldsymbol{t}}^{*}(\boldsymbol{\mu}[\boldsymbol{k}]), \tag{4-6}$$

where the path index is omitted. In this paper, we assume that AoD is already known or does not need to be estimated, and will focus on estimating AoA from the remaining content.

Similar to [VVH16], we adopt a Gaussian process noise model for the AoA evolution over the time, given by

$$\boldsymbol{\phi}[\boldsymbol{k}+\mathbf{1}] = \boldsymbol{\phi}[\boldsymbol{k}] + \boldsymbol{\xi}[\boldsymbol{k}], \tag{4-7}$$

where $\xi[k]$ is zero-mean Gaussian noise distributed $\mathcal{N}(0, \sigma^2)$, and σ^2 denotes the AoA variation in one time slot. The evolution model for path gain is given by the first-order Gauss-Markov model

$$\boldsymbol{\alpha}[\boldsymbol{k}+\mathbf{1}] = \boldsymbol{\rho}\boldsymbol{\alpha}[\boldsymbol{k}] + \boldsymbol{\varepsilon}[\boldsymbol{k}], \tag{4-8}$$

where ρ is the correlation coefficient, and $\varepsilon[k]$ is zero-mean complex Gaussian noise distributed $\mathcal{CN}(0, (1-\rho)^2)$. The received signal after combining can be expressed as

$$\boldsymbol{y}[\boldsymbol{k}] = \boldsymbol{\alpha}[\boldsymbol{k}] \cdot \mathrm{w}_{\boldsymbol{r}}^{*}\boldsymbol{\alpha}[\boldsymbol{k}]\mathrm{a}_{\boldsymbol{r}}(\boldsymbol{\psi}[\boldsymbol{k}])\mathrm{a}_{\boldsymbol{t}}^{*}(\boldsymbol{\mu}[\boldsymbol{k}])\mathrm{f}_{\boldsymbol{t}} \cdot \boldsymbol{x}[\boldsymbol{k}] + \mathrm{w}_{\boldsymbol{r}}^{*}\mathrm{n}, \tag{4-9}$$

where $\mathbf{f}_t \in \mathbb{C}^{N\times 1}$ is beamformer, $\mathbf{w}_r \in \mathbb{C}^{M\times 1}$ is combiner, $\mathbf{n} \in \mathbb{C}^{M\times 1}$ is the zero-mean complex white Gaussian noise vector, and $x[k]$ is a transmit symbol.

4.1.1 An Overview of ABP Design for Angle Estimation

Recently, Zhu et al. [ZCH17] propose ABP for angle estimation, assuming a narrowband single-path channel with ULAs equipped at both the transmitter and receiver. Each ABP consist of two continuous DFT-based analog beams in both time and angular domains as shown in Figure 4.1-2. In [ZCH17], full steering are required by the receiver to simultaneously estimate the singlepath AoA. The angle estimation algorithm using ABP is as follows. First, the RSS is calculated by using all the beams, and two consecutive beams are selected. One has the largest RSS and another has the second largest RSS. The received signals of the two selected beams are derived as

$$y_m^{\Delta} = \alpha\mathbf{a}_r^{*}(\eta_m - \delta_r)\mathbf{a}_r(\psi)\mathbf{a}_t^{*}(\mu)\mathbf{f}_t x + \mathbf{a}_r^{*}(\eta_m - \delta_r)\mathbf{n} \text{ and}$$
$$y_m^{\Sigma} = \alpha\mathbf{a}_r^{*}(\eta_m + \delta_r)\mathbf{a}_r(\psi)\mathbf{a}_t^{*}(\mu)\mathbf{f}_t x + \mathbf{a}_r^{*}(\eta_m + \delta_r)\mathbf{n},$$

where η_m is the boresight angle of the m-th receive ABP, and $\delta_r = \frac{\pi}{N_{\mathrm{tot}}}$ is approximates the half of half-power beamwidth for the receiver. The RSSs calculated from the received signals of the two beams are derived as

$$\boldsymbol{\chi}_{\boldsymbol{m}}^{\boldsymbol{\Delta}} = (\boldsymbol{y}_{\boldsymbol{m}}^{\boldsymbol{\Delta}})^{*}\boldsymbol{y}_{\boldsymbol{m}}^{\boldsymbol{\Delta}} \textbf{ and } \boldsymbol{\chi}_{\boldsymbol{m}}^{\boldsymbol{\Sigma}} = (\boldsymbol{y}_{\boldsymbol{m}}^{\boldsymbol{\Sigma}})^{*}\boldsymbol{y}_{\boldsymbol{m}}^{\boldsymbol{\Sigma}}. \tag{4-10}$$

The ratio metric is defined as

$$\boldsymbol{\zeta}_{\boldsymbol{m}}^{\mathbf{AoA}} = \frac{\boldsymbol{\chi}_{\boldsymbol{m}}^{\boldsymbol{\Delta}} - \boldsymbol{\chi}_{\boldsymbol{m}}^{\boldsymbol{\Sigma}}}{\boldsymbol{\chi}_{\boldsymbol{m}}^{\boldsymbol{\Delta}} + \boldsymbol{\chi}_{\boldsymbol{m}}^{\boldsymbol{\Sigma}}} = -\frac{\mathbf{sin}(\boldsymbol{\psi}-\boldsymbol{\eta}_{\boldsymbol{m}})\,\mathbf{sin}(\boldsymbol{\delta}_{\boldsymbol{r}})}{\mathbf{1}-\mathbf{cos}(\boldsymbol{\psi}-\boldsymbol{\eta}_{\boldsymbol{m}})\,\mathbf{cos}(\boldsymbol{\delta}_{\boldsymbol{r}})}.. \tag{4-11}$$

In [ZCH17], it was proved that ζ_m^{AoA} is a monotonically decreasing function of ψ, and thus there exists an inverse function. The estimated value of ψ can be recovered by using the inverse function.

4.1.2 Proposed beam tracking algorithm

ABP-EKF beam tracking algorithm is proposed to improve the tracking performance. First, we explain the modified ABP structure, which overcomes estimation performance degradation for estimating the

AoA near the boundary of ABP probing range, and we propose the EKF algorithm which utilizes the ratio metric of ABP as a measurement function.

In [ZCH17], the authors propose algorithm that has good AoA estimation performance in high SNR region. As shown in Figure 4.1-2, the two beams numbered ① and ② represent the m-th receive ABP, and the main probing range of the m-th receive ABP denotes$[\eta_m - \delta_r, \eta_m + \delta_r]$. We define the the *delta beam* and *sum beam* of m-th receive ABP are steered towards $(\eta_m - \delta_r)$, $(\eta_m + \delta_r)$, respectively. The sum beam $\mathbf{a}_r(\eta_m + \delta_r)$ numbered ② has the largest RSS, and the delta beam $\mathbf{a}_r(\eta_m - \delta_r)$ numbered ① has the second largest RSS. The beam with the true second largest RSS is the beam numbered ①, but the beam numbered ③ is selected as the second largest RSS because of noise. Then the AoA is estimated using $(m + 1)$-th ABP whose probing range does not include AoA. This mismatch occurs frequently at the low SNR. As you can see in Figure 4.1-2, the effect of noise is severe when the AoA is near the boundary of ABP probing range. Therefore we propose modified ABP structure with better AoA estimation performance.

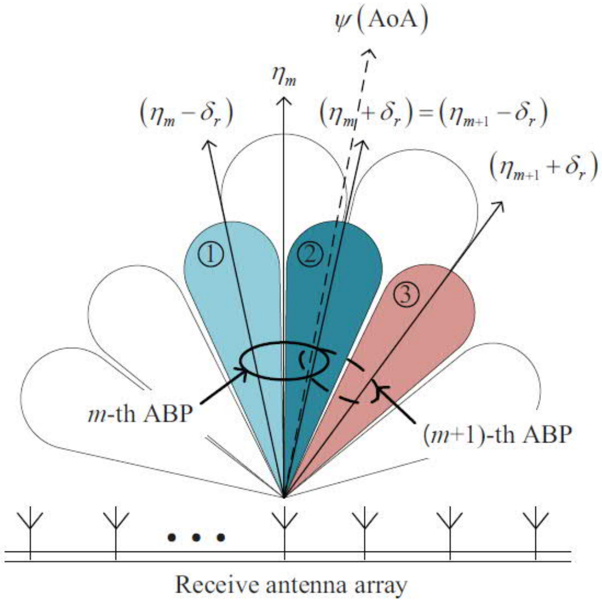

Figure 4.1-2 A conceptual example of receive auxiliary beam pair structure.

To prevent ABP wrong selection for estimating the AoA near the boundary of ABP probing range, we use additional ABP hatched as shown in Figure 4.1-3. Prior to describe additional ABP, we define the estimation trust region of ABP using the following characteristics of the ratio metric. The ratio metric of ABP belongs to $[-1, 1]$ in the range between the steering angles of the delta beam and sum beam as shown in Figure 4.1-4. Therefore, the estimation trust region of ABP is defined based on the value of ratio metric excluding the boundary region of probing range as follows:

$$\boldsymbol{\Omega}_{\mathbf{tr}} = \{\boldsymbol{\zeta} | \boldsymbol{\zeta}_{\mathbf{low}} \le \boldsymbol{\zeta} \le \boldsymbol{\zeta}_{\mathbf{up}}\}, \qquad (4\text{-}12)$$

where $\zeta_{\mathrm{low}} = -\zeta_{\mathrm{up}} = -\frac{\sin\left(\frac{\delta_r}{2}\right)\sin(\delta_r)}{1-\cos\left(\frac{\delta_r}{2}\right)\cos(\delta_r)}$.

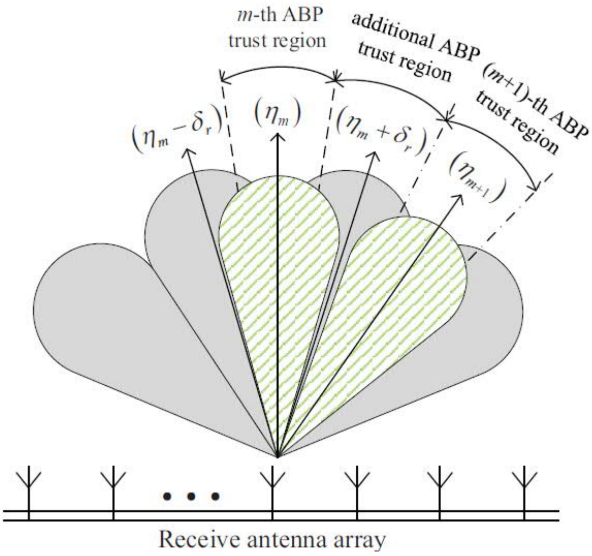

Figure 4.1-3 An example of additional auxiliary beam pair to estimate AoA outside the estimation trust region.

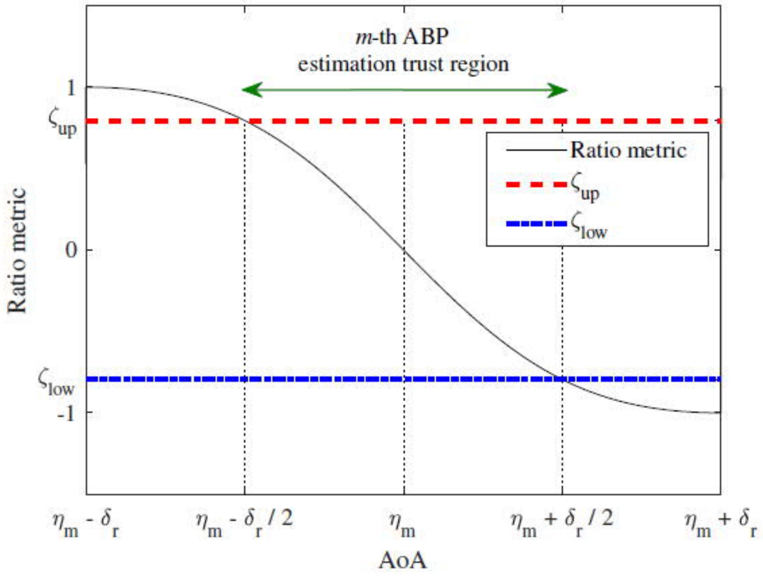

Figure 4.1-4 The ratio metric of m-th ABP versus AoA.

If the value of ratio metric is not in the estimation trust region, i.e., $\zeta_{\mathrm{low}} < \zeta$ or $\zeta_{\mathrm{up}} < \zeta$, additional ABP, whose boresight angle is shifted, should be used to estimate the AoA. The conditions for changing the boresight angle of ABP are as follows:

$$\boldsymbol{\eta} = \begin{cases} \boldsymbol{\eta_m + \delta_r} & \textbf{if } \boldsymbol{\zeta < \zeta_{\mathrm{low}}} \\ \boldsymbol{\eta_m - \delta_r} & \textbf{if } \boldsymbol{\zeta_{\mathrm{up}} < \zeta} \end{cases}. \tag{4-13}$$

For example, assume that the m-th ABP is used to estimate the AoA. If AoA to be estimated is within $\left[\eta_m + \frac{\delta_r}{2}, \eta_m + \delta_r\right]$ i.e., $\zeta < \zeta_{\mathrm{low}}$ as shown in Figure 4.1-4, then the ABP for the AoA estimation is changed to ABP consisting of additional beams from the m-th ABP. In other words, ABP to estimate AoA are switched from m-th ABP to hatched ABP in Figure 4.1-3.

By using the modified ABP structure with the condition in (4-13), the AoA to be estimated almost exists in the estimation trust region, we can avoid the ABP wrong selection. Therefore, although it may be necessary to obtain one more RSS of a modified ABP based on the trust region, the performance degradation of the existing ABP algorithm can be overcomed.

4.1.3 AoA tracking via extended Kalman filter

The mmWave system is essential for beamforming to overcome high path loss. Considering the mobile environments, accurate and frequent beam training is mandatory due to the rapid changes of the channel. Multiple singal classification (MUSIC) and conventional beam estimation algorithms by using full steering with high complexity are unsuitable in fast varying channel. Therefore, beam tracking algorithm with low complexity and high performance becomes important in mobile environments. The EKF, widely known as MMSE tracker, can be used for beam tracking with low complexity.

We propose beam tracking algorithm that combines EKF with modified ABP structure. In order to implement EKF, we need a dynamic state model for the AoA. We model the state evolution of parameter ϕ from the k-th received signal to $(k+1)$-th one as

$$\boldsymbol{\phi}(\boldsymbol{k}+\mathbf{1}) = \boldsymbol{\phi}(\boldsymbol{k}) + \boldsymbol{\xi}(\boldsymbol{k}), \tag{4-14}$$

where $\xi(k)$ is a zero-mean Gaussian noise with variance σ^2. We define the measurement equation as ratio metric of ABP as follows:

$$\underbrace{\zeta_m^{\mathrm{AoA}}(k)}_{z(k)} = -\underbrace{\frac{\sin(\psi(k)-\eta_m)\sin(\delta_r)}{1-\cos(\psi(k)-\eta_m)\cos(\delta_r)}}_{h(\phi(k))} + \tau(k), \tag{4-15}$$

where $\psi(k) = \frac{2\pi}{\lambda} d_r \sin\phi(k)$, and $\tau(k)$ is a zero-mean Gaussian noise with variance σ_τ^2. The EKF equations are given as following [RSP+14]

- The time update equations:

$$\hat{\phi}(k|k-1) = \hat{\phi}(k-1|k-1), \tag{4-16}$$

$$P(k|k-1) = P(k-1|k-1) + \sigma^2. \tag{4-17}$$

- Jacobian:

$$H(k) = \left.\frac{\partial h}{\partial\phi(k)}\right|_{\phi(k)=\hat{\phi}(k|k-1)}.. \tag{4-18}$$

- Innovation value $S(k)$:

$$S(k) = \sigma_\tau^2 + H(k)P(k|k-1)H(k)^{\mathrm{T}}.. \tag{4-19}$$

- Kalman gain $K(k)$:

$$K(k) = P(k|k-1)H(k)^{\mathrm{T}}S(k)^{-1}.. \tag{4-20}$$

- The measurement update equation:

$$\hat{\phi}(k|k) = \hat{\phi}(k|k-1) + K(k)\Big(z(k) - h\big(\hat{\phi}(k|k-1)\big)\Big),. \tag{4-21}$$

$$P(k|k) = \big(1 - K(k)H(k)\big)P(k|k-1).. \tag{4-22}$$

The purpose of EKF is to track the AoA from the measurement as ratio metric of ABP, recursively. In (4-16) and (4-17), a priori state $\hat{\phi}(k|k-1)$ and a priori error covariance $P(k|k-1)$ are predicted in accordance with state evolution model in (4-14), where σ^2 is the state noise variance and σ_τ^2 is the measurement error variance. In (4-15), we can see that measurement model is nonlinear in the state parameter. To implement EKF, we can linearize measurement model by using Jacobian in (4-18).

In what follows we evaluate the performance of the proposed beam tracking algorithm in mobile environments. The operating frequency $f_c = 28\,\mathrm{GHz}$, and both BS and MS employ ULAs with distance between adjacent antenna elements d = $\frac{\lambda}{2}$, and the total number of antenna at the transmitter and receiver are set to be $N = 8$ and $M = 8$. We consider that time-slots is 45 ms for beam training period in outdoor mmWave channel model [RSP+14]. Therefore, the mobility 0.25° per time-slot is equal to $5.56°/s$, as increasing distance between MS and BS, and it can be modeled as a high mobility environments. Suppose the distance MS and BS is 300 m. This model can then be considered to move the MS at 104 km/h, approximately.

We compare proposed ABP-EKF algorithm to the results of ABP algorithm [ZCH17] and MUSIC algorithm [S81]. MUSIC algorithm has a good estimation performance, but large overhead is required to obtain the accurate received signal covariance matrix. In Figure 4.1-5, we provide the snapshots of the angle tracking performance over time for angle variation $\sigma^2 = (0.25°)^2$ at $\mathrm{SNR} = 5\,\mathrm{dB}$. In ABP based AoA estimation technique, when ABP switches as angle changes, ABP is incorrectly selected due to noise, and angle estimation performance degradation occur. Whereas, the modified ABP-based algorithm for estimating angles with additional ABP outside the angle estimation trust region of ABP shows improved estimation performance. At $\mathrm{SNR} = 5\,\mathrm{dB}$, we can see that the AoA tracking performance of modified ABP algorithm is comparable to the MUSIC algorithm's performance.

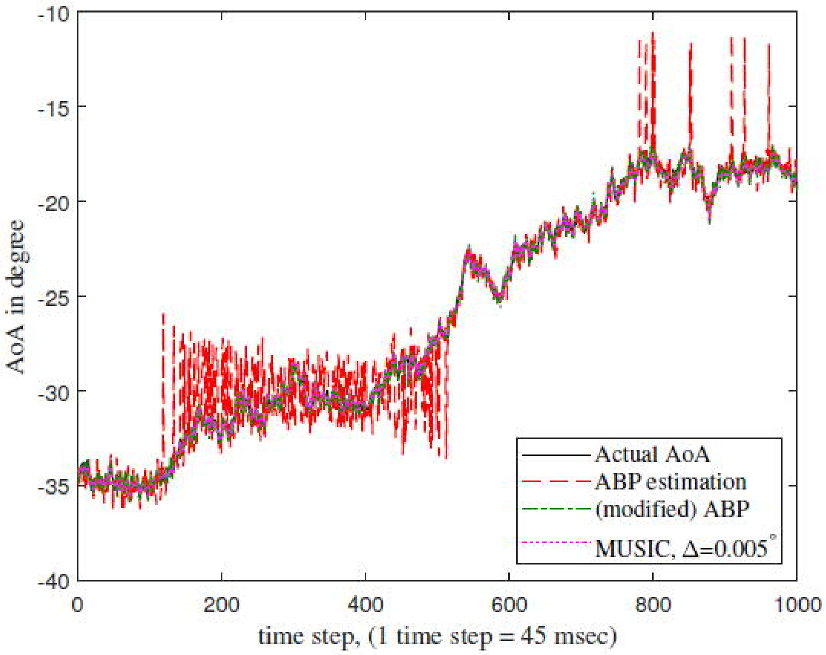

Figure 4.1-5 AoA tracking versus time index at SNR = 5 dB and $\sigma^2 = (0.25°)^2$.

In Figure 4.1-6, we compare the probability of ABP selection failure for AoA estimation between ABP estimation and modified ABP estimation. The probability of ABP selection failure means that no valid ABP is selected to estimate the true AoA. In ABP estimation algorithm, ABP selection failure may occur for AoA estimation near the ABP probing range boundary at all SNRs. On the other hand, in modified ABP estimation algorithm, which changes ABP to estimate AoA based on the trust region, ABP selection failure is reduced as SNR increases. Figure 4.1-7 shows the MSE performance of the proposed beam tracking algorithm, ABP algorithm in [ZCH17] and MUSIC algorithm in [S81] at different SNRs. In the MUSIC algorithm, the candidate angle interval for angle estimation is set to $\Delta = 0.005°$. Figure 4.1-7 shows the results of tracking through angle estimation algorithms when the angle variation is $\sigma^2 = (0.01°)^2, (0.25°)^2$ in the AoA model. As the angle variation increases, the proposed ABP-EKF algorithm's tracking performance degradation occurs. As the EKF tracks the stochastic characteristics of the AoA variation model, this angular noise remains in the tracking results as the angular variation increases over time. However, we can see better tracking performance compared to traditional algorithm such as MUSIC and ABP based angle estimation techniques in low SNR region. For example, the MSE of ABP algorithm, MUSIC and proposed ABP-EKF algorithm are $1.0, 4.6 \times 10^{-2}, 3.2 \times 10^{-2}$ at $\mathrm{SNR} = 10\,\mathrm{dB}$, respectively.

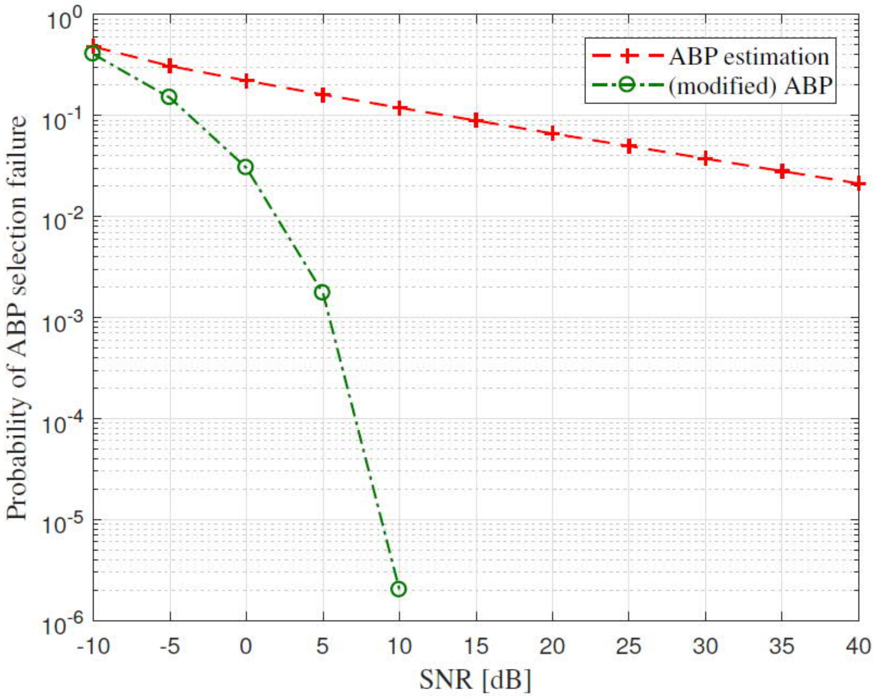

Figure 4.1-6 Probability of ABP selection failure under various SNR levels.

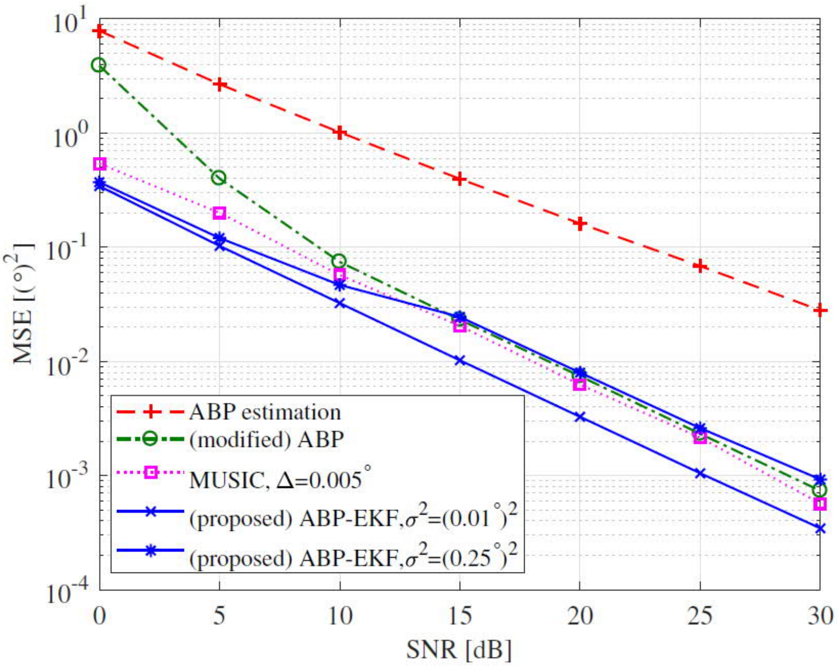

Figure 4.1-7 MSE of the angle defined by $\mathrm{E}\left[\left|\phi[k] - \phi\,[\widehat{k}]\right|^2\right]$ under various SNR levels.

4.2 Lens antenna-based performance assessment of beamforming

Introduction

In this section, we analyze the difference between BS with hybrid beamforming RF lens antenna and beamforming with phase shifters that is the conventional beamforming method. Our purpose in this study is to find the reason to make beam-squint (BQ) in the RF lens antenna, suggest the compensation method of BQ. In WP2, use cases focus on firefighting with drones and robots. To supporting fast-moving objects, drones, beam-tracking of BS is significantly essential. In mmWave, Lens antenna with lower hardware cost and fewer RF chains than phased array has been studied for beamforming and beam tracking. RF Lens based system is as follows,

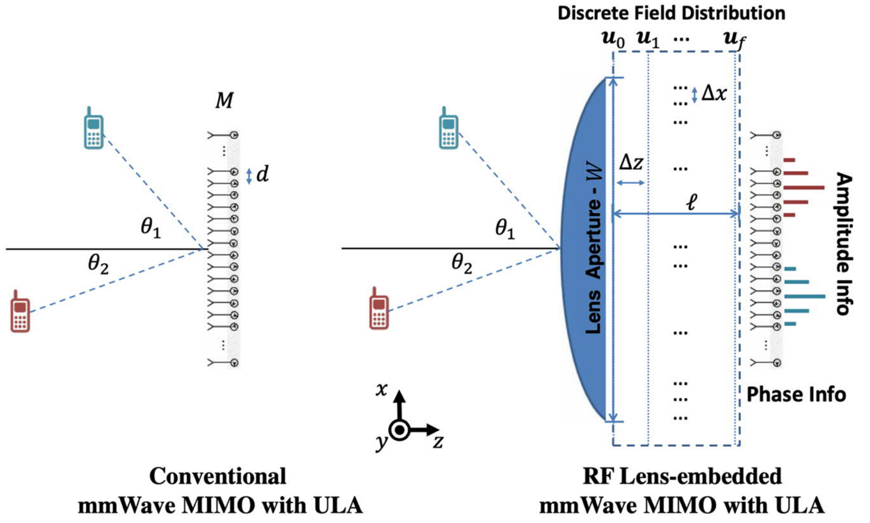

Conventional mmWave MIMO with ULA

RF Lens-embedded mmWave MIMO with ULA

Figure 4.2-1 A schematic of a multi-user mmWave MIMO system without/with RF lens

In the lens antenna system, we study the beam-squint phenomenon that is not considered before and system performance degradation. In a phased array antenna, the beam-squint means that the transmission angle and direction of the analog beamforming of the antenna are changed depending on the operating frequency [IT95]. The performance degradation by beam squint is much more critical as beamwidth is more narrow by becoming massive MIMO. However, because the reasons for BQ are different btw the RF lens and phased array, we analyze the reason and impact of beam squint, respectively.

4.2.1 Lens Material

For the lens, based on the Lorenz model, an electromagnetic wave is refracted while passing through the inside of the dielectric lens by a refractive index expressed as a dielectric constant. This phenomenon is caused by the fact that the dielectric is a function of frequency, which causes beam-squint phenomena like existing an antenna array with phase shifters. The permittivity equation is as follows [4-2-2].

$$\epsilon_r = \dot{\epsilon}_r + i\ddot{\epsilon}_r = 1 + \omega_p \sum_i \frac{f_i}{\omega_i^2 - \omega^2 - j\omega\gamma_i}$$

ϵ_r is a permittivity and dielectric constant of a dielectric lens, ω_p is the characteristic of the lens, such as a molar mass, density, and the number of electrons per molecular. f_i is the fraction of electrons, γ_i is a damping constant, ω_i is a resonant frequency, ω is an angular frequency.

As is shown in the permittivity equation, permittivity is a function of frequency by angular frequency. However, permittivity is not linear due to damping constant and resonant frequency. These values are inherent values of the material, so accurate values are obtained by the experimental method. Permittivity consists of the real and imaginary parts. To describe permittivity, the real part called by dielectric constant, tangent loss is the ratio of real and imaginary part and as follows [L65];

$$Tangent\ loss = \frac{\dot{\epsilon}_r}{\ddot{\epsilon}_r}.$$

Also, the refractive index that makes the beam refracted in the lens can be expressed as permittivity.

$$n = \dot{n} + i\ddot{n} = \sqrt{\frac{\sqrt{\dot{\epsilon}_r{}^2 + \ddot{\epsilon}_r{}^2} + \dot{\epsilon}_r}{2}} + i\sqrt{\frac{\sqrt{\dot{\epsilon}_r{}^2 + \ddot{\epsilon}_r{}^2} - \dot{\epsilon}_r}{2}}$$

n is the refractive index. The refractive index depends on the permittivity in the following equation. As a result, it is the real part of the refractive index that the beam is refracted. The permittivity influences the real part of the refractive index, and the other frequency band passes through the same material, but the degree of refraction becomes different. This result causes the beam-squint at the lens.

As in the refractive index equation, due to permittivity changes refractive index, From a beam-squint point of view, it is advantageous to have less variation in the values of the dielectric constant and tangent loss in the operating frequency band than to be large and small in permittivity. Therefore, in the lens-based beamforming system, it is essential to select the material of lens with less variation in permittivity.

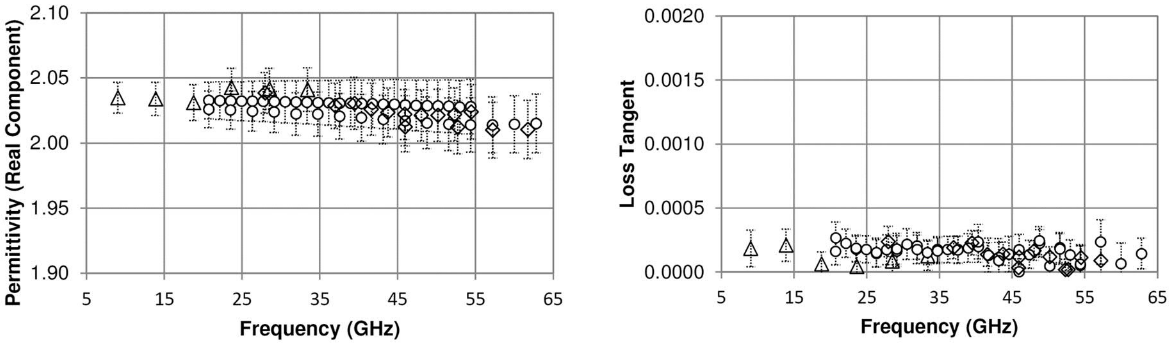

Figure 4.2-2 Directric constant and tangent loss of ***Teflon type A*** [4-2-3]

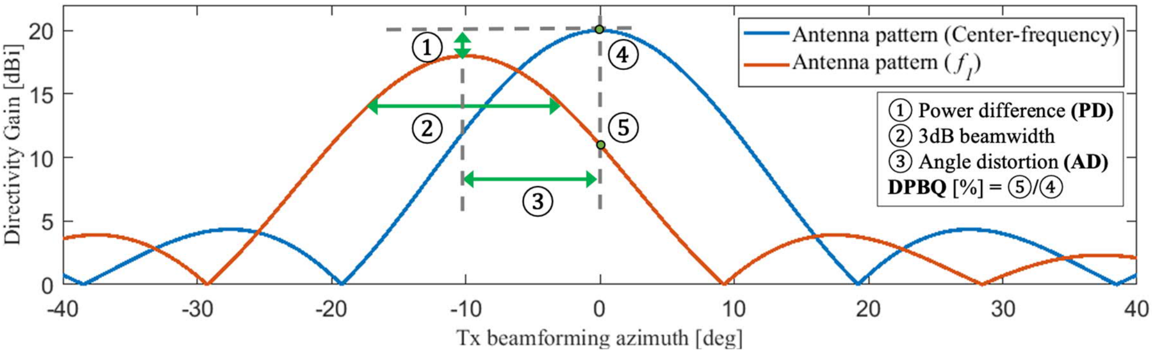

Figure 4.2-3 Relation between PD, AD, BW and DPBQ

In a previous study, five materials of a lens are considered, such as Teflon, polyethylene, polycarbonate, BN, MgO. We considered a material that has unvaried dielectric constant and tangent loss. The lens material used in the simulation was Teflon type A. According to the equation of permittivity and refractive index, the refractive index of the lens must be a function related to frequency, and the material to be used in the manufacture of the lens should take into account the beam-squint phenomenon, so that the real and the imaginary parts of the dielectric will not vary significantly by frequency. Figure 4.2-2 shows the permittivity and tangent loss for the frequency of Teflon type A provided by DuPont Inc [G15]. Tangent loss is the ratio expressed in the real part and imaging part of permittivity. The permittivity value of Teflon type A is about 2.03 in broadband, and the loss tangent value changes from 0.000147 to 0.000216. As such, Teflon has a small loss tangent value and has not much-changed permittivity and loss tangent value at 27 to 30 GHz. These characteristics of Teflon work in favor of the lens, in terms of the beam-squint.

4.2.2 *Parameters & Degraded Power over Beam-sQuint for Analysis*

To assess the BQ phenomenon, we introduce several parameters. First is the angle distortion (AD), which means a difference of azimuth angle of peak power on operating frequency and azimuth angle of peak power on the center frequency. However, It is not possible to judge a hazard only by the angle distortion generated by the beam-squint. The most influential parameters are 3dB-beamwidth and power difference (PD). So we need to require the establishment of a new key performance indicator (KPI) as degraded power over beam squint (DPBQ). Figure 4.2-3 describes three parameters used in Eq. DPBQ. First, PD means the difference between peak antenna gain on each operating frequency and peak antenna gain on the center frequency. Second is the 3dB beamwidth of the beam on each frequency band. Beamwidth is the main factor that can affect degradation DPBQ and is affected by the array size. Larger array size makes the beam narrower and being critical degradation. Equation DPBQ is as follows;

$$DPBQ\ [\%] = \frac{(Gain(28.5GHz) - PD)\left|sinc(0.6238\,\frac{AD}{3dB\ Beamwidth})\right|}{Gain(28.5GHz)} \times 100$$

In the definition of DPBQ, the antenna pattern is assumed as a sinc function. DPBQ represents the percentage of the ratio antenna gain on center frquency to distorted antenna gain on the operating frequency. For example, what DPBQ is 80% on 27GHz means antenna gain ratio of antenna gain of the center frequency to antenna gain of 27GHz at undistorted azimuth angle is 80%. Because DPBQ estimates degraded power with three parameters only, DPBQ is useful in a situation where the entire antenna pattern can be unknown such as link-level simulation.

Table 4.2-2 Case 1 (Ca1). -> Case 2 (Ca2). Angle Distortion (AD) value [dBi] at 10 λ diameters

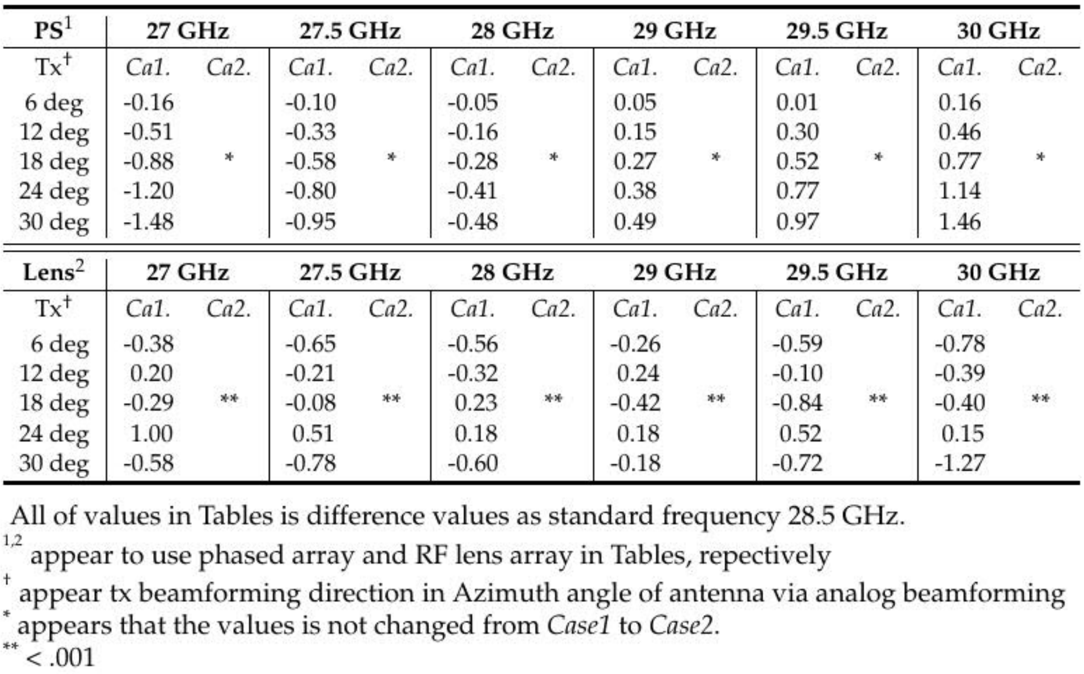

PS[1]	27 GHz		27.5 GHz		28 GHz		29 GHz		29.5 GHz		30 GHz	
Tx†	*Ca1.*	*Ca2.*	*Ca1.*	*Ca2.*	*Ca1.*	*Ca2.*	*Ca1.*	*Ca2.*	*Ca1.*	*Ca2.*	*Ca1.*	*Ca2.*
6 deg	-0.16		-0.10		-0.05		0.05		0.01		0.16	
12 deg	-0.51		-0.33		-0.16		0.15		0.30		0.46	
18 deg	-0.88	*	-0.58	*	-0.28	*	0.27	*	0.52	*	0.77	*
24 deg	-1.20		-0.80		-0.41		0.38		0.77		1.14	
30 deg	-1.48		-0.95		-0.48		0.49		0.97		1.46	

Lens[2]	27 GHz		27.5 GHz		28 GHz		29 GHz		29.5 GHz		30 GHz	
Tx†	*Ca1.*	*Ca2.*	*Ca1.*	*Ca2.*	*Ca1.*	*Ca2.*	*Ca1.*	*Ca2.*	*Ca1.*	*Ca2.*	*Ca1.*	*Ca2.*
6 deg	-0.38		-0.65		-0.56		-0.26		-0.59		-0.78	
12 deg	0.20		-0.21		-0.32		0.24		-0.10		-0.39	
18 deg	-0.29	**	-0.08	**	0.23	**	-0.42	**	-0.84	**	-0.40	**
24 deg	1.00		0.51		0.18		0.18		0.52		0.15	
30 deg	-0.58		-0.78		-0.60		-0.18		-0.72		-1.27	

All of values in Tables is difference values as standard frequency 28.5 GHz.

[1,2] appear to use phased array and RF lens array in Tables, repectively

† appear tx beamforming direction in Azimuth angle of antenna via analog beamforming

* appears that the values is not changed from *Case1* to *Case2*.

** < .001

Table 4.2-1 Case 1 (Ca1). -> Case 2 (Ca2). Power difference (PD) value [deg] at 10 λ diameters.

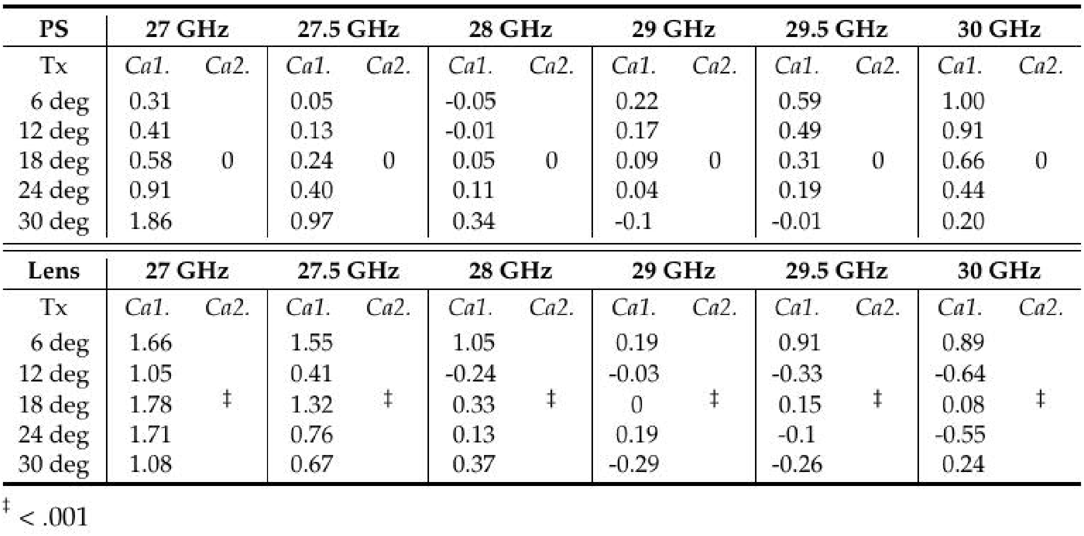

PS	27 GHz		27.5 GHz		28 GHz		29 GHz		29.5 GHz		30 GHz	
Tx	*Ca1.*	*Ca2.*	*Ca1.*	*Ca2.*	*Ca1.*	*Ca2.*	*Ca1.*	*Ca2.*	*Ca1.*	*Ca2.*	*Ca1.*	*Ca2.*
6 deg	0.31		0.05		-0.05		0.22		0.59		1.00	
12 deg	0.41		0.13		-0.01		0.17		0.49		0.91	
18 deg	0.58	0	0.24	0	0.05	0	0.09	0	0.31	0	0.66	0
24 deg	0.91		0.40		0.11		0.04		0.19		0.44	
30 deg	1.86		0.97		0.34		-0.1		-0.01		0.20	

Lens	27 GHz		27.5 GHz		28 GHz		29 GHz		29.5 GHz		30 GHz	
Tx	*Ca1.*	*Ca2.*	*Ca1.*	*Ca2.*	*Ca1.*	*Ca2.*	*Ca1.*	*Ca2.*	*Ca1.*	*Ca2.*	*Ca1.*	*Ca2.*
6 deg	1.66		1.55		1.05		0.19		0.91		0.89	
12 deg	1.05		0.41		-0.24		-0.03		-0.33		-0.64	
18 deg	1.78	‡	1.32	‡	0.33	‡	0	‡	0.15	‡	0.08	‡
24 deg	1.71		0.76		0.13		0.19		-0.1		-0.55	
30 deg	1.08		0.67		0.37		-0.29		-0.26		0.24	

‡ < .001

Description & evaluation

In this section, for each antenna index, measure the angle distortion of each frequency band relative to the center frequency. This angle distortions are compared with the phased shift array, which is a conventional analog beamforming method. For an accurate analysis of the BQ phenomenon, we set two cases. Case 1 takes into account only Assumption 1. Case 2 considers Assumption 1 and 2. The assumptions are as follows;

Assumption 1. The factor that affects beam refraction is the only refractive index that is a function of permittivity.

Assumption 2. The beam pattern of the antenna behind the RF lens is the same on the system bandwidth.

Assumption 1 is designated to eliminate the likelihood of intervention by other variables in the refractive index. Assumption 2 removes the distorted component according to the beam pattern of the antenna that does not support wideband. With the following assumptions, case 1 is a realistic situation, and case 2 assumes an ideal situation. In case 2, we can observe the beam-squint phenomenon by the dielectric constant and tangent loss of material only in the lens by adding assumption 2.

A. Case 1: Assumption 1

Case1 was measured in the patch antenna, which does not support wide bandwidth, with the only assumption 1 considered.

Table 4.2-2 shows the AD values corresponding to each frequency for each analog beamforming direction. As a result, PS tends to increase AD as the scanning angle increases. This means that the beam-squint phenomenon at the maximum scanning angle of the fixed antenna array is most critical. AD ranges from -1.48 to 1.46, especially at 30deg. As explained in the introduction, AD of PS is caused by a weighted vector aligned at 28.5 GHz for analog beamforming.

In contrast, AD of RF lens isn't worse more than PS, but unlike PS, it is difficult to identify the existence of trends relative to each frequency. First, the factor affecting AD of a lens is permittivity that is changed depending on the frequency described earlier. The second factor is the pattern of the patch antenna. In the lens in Case 1, these two problems come together. Case 2 classifies the difference of two parameters. Table 4.2-1 shows PD values in the same situations shown in Table 4.2-2. Unit is dB. Table 4.2-1 shows no significant difference in PD values of PS except 1 dB of (30 GHz, 6deg) and 1.86 dB of (27 GHz, 30deg). The lens has a considerable PD value overall, but only more frequent than PS, and the maximum difference is similar. A common cause for PD is a single antenna beam pattern, and In lens, tangent loss, which further varies with frequency, is an additional factor. The PD values in Case 1 are the values changed by both the tangent loss and the beam pattern of a single patch antenna. The lens does not use multiple patch antennas, such as PS, for analog beamforming, and use one or a subset of antennas. Therefore, the lens that is more affected by a single antenna pattern is more vulnerable from a PD perspective than PS.

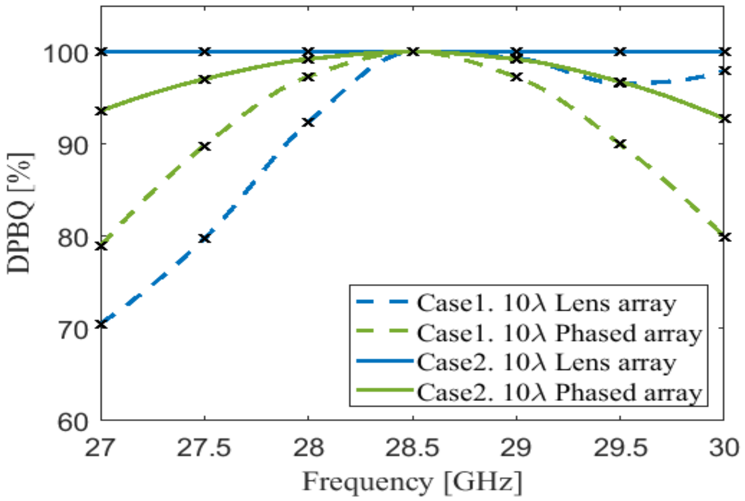

Figure 4.2-4 Degraded power over beam-squint (DPBQ)

B. Case 2: Assumption 1, 2

Case 2 adds assumption 2 in case 1 so that only the AD and the PD phenomenon of the lens can be checked for changes in the permittivity of the material. Because the attenuation in the lens is based on tangent loss, the PD values change according to the varying tangent loss value over frequency. In Table 4.2-2, we can confirm that PS has the same value as Case 1. This is because the AD of PS is only affected by the weighted vector. In the case of a lens, AD values are less than 0.001. In other words, AD due to the changes in permittivity can be negligible, and single patch antenna beam pattern causes the most of AD. Besides, from the PD perspective of Table 4.2-1, the PD value of the lens converges into zero, so we can see that by choosing materials with little variation, such as Teflon, it is rarely distorted by the characteristics of the lens itself.

C. Degraded power over beam-squint (DPBQ)

Overall, Figure 4.2-4 shows DPBQ values for frequency. Case 1 shows PS reduced performance up to 20 percent due to the influence of more robust AD and PD. For lenses, DPBQ is much worse as up to 30 percent of degraded performance. This result can be concluded that PS is more robust than the lens from the perspective of AD and PD shown earlier. In both cases, however, it creates a performance degradation that cannot be ignored.
On the other hand, in Case 2, the DPBQ of the lens has 100 percentage values without degradation, with both AD and PD having no distortion. This result means that the lens antenna is not structurally affected by BQ. In case 2 of PS, there is a degradation of up to 7 percent.

Ongoing research for D3.3

We will continuously add 20λ diameters cases of the lens and phased array, respectively, to check the degraded performance in large size antenna. Also, we assess throughput assessment via real 3D-map raytracing.

4.3 Hybrid Beamforming Based on Monopuse Ratio

Hybrid analog/digital precoding is a promising technology for millimeter wave (mmWave) multi-user multiple-input multiple-output (MIMO) communications. In hybrid analog/digital precoding, the severe path loss characteristic of mmWave frequencies is compensated by analog radio-frequency (RF) directional precoding/combining utilizing array gains. Moreover, multi-user interference can be flexibly suppressed by digital baseband (BB) precoding. As a new feature for the 5G NR mmWave systems, designing RF precoder/combiner faces significant challenges, such as establishing accurate directional radio links and maintaining the links, while mobile stations (MSs) are moving in outdoor environments.

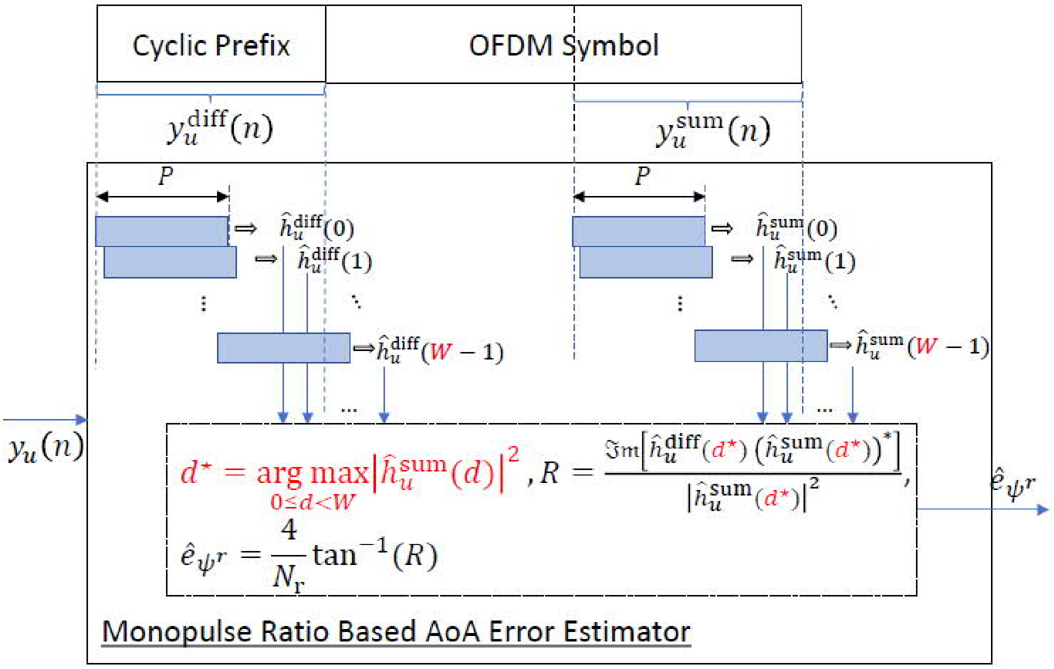

Figure 4.3-1 Monopulse Ratio Based AoA Error Estimator.

For two-stage multi-user hybrid precoding, the conventional solution first selects the RF precoders/combiners by codebook-based beam sweeping and then determines BB precoders, but this method cannot fully exploit the array gain due to finite grid of RF beam codebooks and avoid nonnegligible sounding protocol overheads of measuring adjacent candidate beam pairs. In this deliverable, a novel solution is presented, which consists of low sounding overhead beam tracking protocol, monopulse ratio-based receiver structure, and fine accuracy AoA/AoD error estimation algorithm. What makes our solution unique is the receiver structure for AoA/AoD error estimation, which is inspired by the monopulse ratio used in radar systems. The proposed solution integrates monopulse ratio-based AoA/AoD estimators within only one orthogonal frequency division multiplexing (OFDM) symbol utilizing the cyclic prefix in OFDM symbols, achieving more accurate beam acquisition and much lower sounding overheads in beam tracking protocols than the conventional solution. Furthermore, the proposed solution is suitable for MSs with a single RF chain.

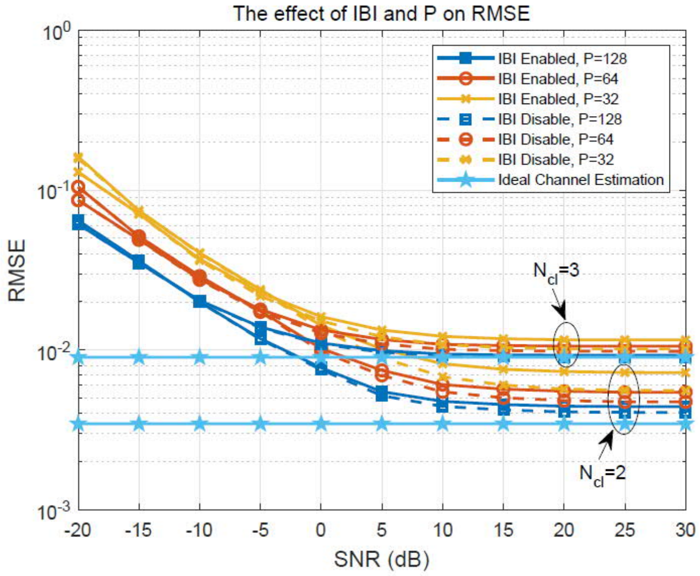

Figure 4.3-2 MS AoA Estimatino Performance in RMSE

In **Error! Reference source not found.**, numerical evaluation and computer simulations show that the proposed solution offer more accurate beam acquisition (i.e., average array gain improvement of several dB) as compared to the conventional solution. In addition, a ray-tracing tool is used to demonstrate that the proposed solution works well with significantly lower sounding overheads in beam tracking protocols. In Figure 4.3-3, simulation results show that the proposed hybrid beamfroming achieve spectral efficiency performance that is close to conventional scheme using finest angular resolution.

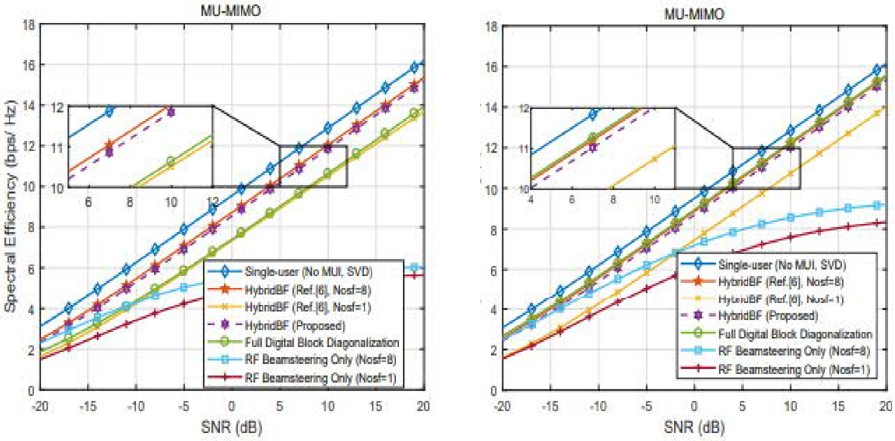

Figure 4.3-3 Beamforming Performance in Spectral Efficiency

Conclusions

The main objective of this deliverable is to provide an intermediate status report about the work that has been conducted as part of work package mmWave radio technologies.

In Section 2, a novel mmWave transceiver architecture based on 5G NR requirements is shown. The components to achieve such as system are characterized, and performance measurements of the complete mmWave front-end with 5G NR compliant PHY layer signals are presented. These results indicate suitable EVM performance for the Primo-5G use cases.

In section 3, first, we designed waveforms and prototype filters for QAM-FBMC considering an MMSE receiver filter. The proposed filters are designed to have a superior self-SINR under the condition of the linear receiver, and we confirmed that the filters show the best performance with the design intent through simulation results. In addition, the formulations of the linear system and self-SINR equations for QAM-FBMC showed a simpler representation than that of the previously complex QAM-FBMC system; therefore, we identified the possibility of applying popular signal processing technology directly to QAM-FBMC in the future. Second, we proposed USFDMA as a new waveform in anticipation that it would be challenging to satisfy the target service condition in D1.1 with OFDMA and GFDM. USFDMA is a suitable waveform to satisfy the URLLC service condition because filtering and resource allocation are possible for each carrier so that it is possible to reduce interference and OOBE and maximize spectral efficiency.

In section 4, first, we proposed a beam tracking algorithm based on ABP-EKF for mmWave MIMO systems in mobile environments. With the modified ABP structure, the proposed algorithm has better beam tracking performance than ABP based angle estimation in the low SNR region, and the MSE performance can be improved by EKF. Second, we analyzed the beam-squint phenomenon in RF lens array and phased array for an ultra-wideband mmWave system. To find the causes of BQ in the RF lens, we separated two cases with assumptions. The leading cause is the antenna beampattern difference of single patch antenna that does not support ultra-wideband if the material of the lens has stable permittivity over frequency. To verify these results, we proposed DPBQ as a KPI. Third, Since the mmWave band has a strong directivity and is vulnerable to blockage, an accurate estimation technique is required for analog beamforming. Conventional techniques require many RF chains to achieve accuracy so that it is difficult to apply. We proposed a technique to estimate the offset by calculating the monopulse ratio using a sum beam and difference beam, respectively, when transmitting data and CP. It showed that it uses lower overhead than the conventional scheme, but can achieve similar performance.

References

[3GPP20-38101] 3GPP Specification 38.101-2 f80, https://www.3gpp.org/ftp/Specs/archive/38_series/38.101-2/38101-2-f80.zip, Jan 2020.

[NI-USRP17] NI USRP-2954-R Manual, http://www.ni.com/pdf/manuals/375725c.pdf, July 2017.

[F46] Friis, H.T. "A Note on a Simple Transmission Formula". IRE Proc.: 254–256, (May 1946).

[BBC+14] P. Banelli, S. Buzzi, G. Colavolpe, A. Modenini, F. Rusek, and A. Ugolini, “Modulation formats and waveforms for 5G networks: Who will be the heir of OFDM?: An overview of alternative modulation schemes for improved spectral efficiency,” IEEE Signal Process. Mag., vol. 31, no. 6, pp. 80–93, Nov. 2014.

[P94] H. V. Poor, An Introduction to Signal Detection and Estimation. New York, NY, USA: Springer, 1994.

[KHP17] H. Kim, H. Han, and H. Park, “Waveform design for QAM-FBMC systems,” in Proc. IEEE 18th Int. Workshop Signal Process. Adv. Wireless Commun. (SPAWC), Jul. 2017, pp. 1–5.

[AD04] C. Audet and J. E. Dennis, Jr., “A pattern search filter method for nonlinear programming without derivatives,” SIAM J. Optim., vol. 14, no. 4, pp. 980–1010, 2004.

[E-UTRA08] Evolved Universal Terrestrial Radio Access (E-UTRA); User Equipment (UE) Radio Transmission and Reception, document 3GPP, 2008.

[YKK+12] Y. H. Yun, C. Kim, K. Kim, Z. Ho, B. Lee, and J.-Y. Seol, “A new waveform enabling enhanced QAM-FBMC systems,” in Proc. IEEE SPAWC, Jul. 2015, pp. 116–120.

[KHP+17] H. Kim, H. Han, and H. Park, “Waveform design for QAM-FBMC systems,” in Proc. IEEE 18th Int. Workshop Signal Process. Adv. Wireless Commun. (SPAWC), Jul. 2017, pp. 1–5.

[VVH16] V. Va, H. Vikalo, and R. W. Heath, “Beam tracking for mobile millimetre wave communication systems,” in IEEE Global Conference on Signal and Information Processing (GlobalSIP), December 2016, pp. 743–747.

[ZCH17] D. Zhu, J. Choi, and R. W. Heath, “Auxiliary beam pair enabled aod and aoa estimation in closed-loop large-scale millimeter-wave MIMO systems,” IEEE Transactions on Wireless Communications, vol. 16, no. 7, pp. 4770–4785, July 2017.

[RSP+14] W. Roh, J. Seol, J. Park, B. Lee, J. Lee, Y. Kim, J. Cho, K. Cheun, and F. Aryanfar, “Millimeter-wave beamforming as an enabling technology for 5G cellular communications: theoretical feasibility and prototype results,” IEEE Communications Magazine, vol. 52, no. 2, pp. 106–113, February 2014.

[S81] R. SCHMIDT, “A signal subspace approach to multiple emitter location and spectral estimation,” Ph. D. Dissertation. Stanford Univ., 1981.

[IT95] Ishii, T. Koryu, ed., “Handbook of microwave technology,” Elsevier, 1995.

[L65] L. Rosenfeld, “Theory of Electrons,” New York: Dover Publications, 68, 1965.

[G15] Glenn Oliver, “Low-Loss Materials in High Frequency Electronics and the Challenges of Measurement,” DuPont, Feb 2015.